

REPORT DOCUMENTATION PAGE					Form Approved OMB No. 0704-0188	
The public reporting burden for this collection of information is estimated to average 1 hour per response, including the time for reviewing instructions, searching existing data sources, gathering and maintaining the data needed, and completing and reviewing the collection of information. Send comments regarding this burden estimate or any other aspect of this collection of information, including suggestions for reducing the burden, to the Department of Defense, Executive Service Directorate (0704-0188). Respondents should be aware that notwithstanding any other provision of law, no person shall be subject to any penalty for failing to comply with a collection of information if it does not display a currently valid OMB control number.						
PLEASE DO NOT RETURN YOUR FORM TO THE ABOVE ORGANIZATION.						
1. REPORT DATE (DD-MM-YYYY) 14-02-2011		2. REPORT TYPE Final Technical		3. DATES COVERED (From - To) 01 Feb 2009 - 30 Apr 2010		
4. TITLE AND SUBTITLE Long-Wave Infrared Semiconductor Negative Refraction Metamaterials for High-Resolution Imaging				5a. CONTRACT NUMBER		
				5b. GRANT NUMBER FA9550-09-1-0029		
				5c. PROGRAM ELEMENT NUMBER		
6. AUTHOR(S) Claire Gmachl				5d. PROJECT NUMBER		
				5e. TASK NUMBER		
				5f. WORK UNIT NUMBER		
7. PERFORMING ORGANIZATION NAME(S) AND ADDRESS(ES) PRINCETON UNIVERSITY 70 PROSPECT AVENUE PRINCETON, NJ 08540				8. PERFORMING ORGANIZATION REPORT NUMBER		
9. SPONSORING/MONITORING AGENCY NAME(S) AND ADDRESS(ES) Air Force Office of Scientific Research 875 N Randolph St Suite 325 Arlington, VA 22203				10. SPONSOR/MONITOR'S ACRONYM(S) AFOSR/RSA		
				11. SPONSOR/MONITOR'S REPORT NUMBER(S) AFRL-OSR-VA-TR-2012-0343		
12. DISTRIBUTION/AVAILABILITY STATEMENT Distribution A: Unlimited						
13. SUPPLEMENTARY NOTES						
14. ABSTRACT The authors have theoretically developed and experimentally verified a set of multilayered metamaterials with negative refraction response spanning the frequency range 8...11 microns (frequency-independent index spanning 8...9.5 microns), leading to the increase of bandwidth of negative refraction by 27%. They also designed and fabricated quantum cascade structures integrated into semiconductor metamaterials; experimental characterization indicates QC action spectrally overlapping with negative refraction region. Finally, the authors theoretically developed a system that is capable of achieving focal spots of the order of 1 micron, and a new analytical technique that can be utilized to image subwavelength objects in the far field.						
15. SUBJECT TERMS "metamaterials" -- "negative refraction" -- "semiconductor" -- "long-wave infrared"						
16. SECURITY CLASSIFICATION OF:			17. LIMITATION OF ABSTRACT	18. NUMBER OF PAGES	19a. NAME OF RESPONSIBLE PERSON	
a. REPORT	b. ABSTRACT	c. THIS PAGE			Dr. Charles Y.-C. Lee	
U	U	U	Unlimited	18	19b. TELEPHONE NUMBER (Include area code)	

Reset

Final report for the award: FA 9550-09-1-0029

“Long-wave infrared semiconductor negative refraction metamaterials for high-resolution imaging”

Executive summary:

Goals of the research:

Metamaterials form a new paradigm for design and development of novel optical and optoelectronics components[1-6]. A new type of metamaterials, semiconductor metamaterials, operating at long-wave-IR frequency range, has been recently proposed and experimentally verified by the team [6-8]. In comparison with other metamaterial designs, semiconductor structures offer the advantages of

- (i) straightforward fabrication that does not require three-dimensional patterning
- (ii) material compatibility with semiconductor technology,
- (iii) relatively low loss that can be further mitigated by electric pumping via quantum cascade (QC) technology

The goals of the project were to assess the perspectives of semiconductor metamaterials for broadband high resolution imaging. Specifically, the project aimed to

- (1) increase operating bandwidth of the metamaterials by combining several layered structures with carefully designed dispersion
- (2) reduce the loss of semiconductor metamaterials by incorporating quantum cascade gain regions into the structure, and
- (3) develop a planar focusing system with sub-wavelength focal spot

Main results:

With relation to the tasks above, we have

- (1) theoretically developed and experimentally verified a set of multilayered metamaterials with negative refraction response spanning the frequency range 8...11 μm (frequency-independent index spanning 8...9.5 μm), leading to the increase of bandwidth of negative refraction by 27%
- (2) designed and fabricated quantum cascade structures integrated into semiconductor metamaterials; experimental characterization indicates QC action spectrally overlapping with negative refraction region
- (3) theoretically developed a system that is capable of achieving focal spots of the order of 1 μm , and a new analytical technique that can be utilized to image subwavelength objects in the far field.

Goal 1: enhancement of bandwidth of negative refraction of metamaterial

The basic principle of operation of our semiconductor metamaterial lies in the collective response of highly-doped plasmonic layers, interlaced by undoped layers, to the incident long-wave infrared (LWIR) light. Since the thickness of individual layer ($\sim 80 \text{ nm}$) in this structure is much smaller than the wavelength of light ($\sim 8 \text{ }\mu\text{m}$), the optical properties of the composite can be described by the effective medium theory. In fact, the collective response of the multilayer is identical to the response of a homogeneous slab with thickness equal to the total thickness of the multilayer with anisotropic dielectric permittivity with components of permittivity tensor given by:

$$\epsilon_{\parallel} = \frac{a_1\epsilon_1 + a_2\epsilon_2}{a_1 + a_2} \dots\dots\dots (1)$$

$$\epsilon_{\perp} = \frac{a_1a_2\epsilon_1\epsilon_2}{a_1\epsilon_2 + a_2\epsilon_1}$$

where a_1, a_2 are the thicknesses of the components of the metamaterial, ϵ_1, ϵ_2 are their permittivities, and ϵ_{\parallel} and ϵ_{\perp} represent the effective permittivity of the metamaterial along and perpendicular to the surface of the layers, respectively.

The typical dispersion of metamaterial is shown in Fig.1. Note that the negative refraction, signified by the condition $\epsilon_{\parallel} > 0, \epsilon_{\perp} < 0$, is limited to the frequencies between the frequency where $\epsilon_1 = 0$ and where $\epsilon_{\parallel} = 0$. Also note that the frequency response of the metamaterial is highly dispersive, i.e. effective permittivities of the metamaterial strongly depend on frequency. Although the design of the metamaterial allows the control of dispersion by adjusting the doping of plasmonic layers, and thus shifting the negative refraction band, the response of the two-component system remains dispersive.

In order to minimize frequency dispersion and to enhance the negative refraction band we designed, fabricated, and verified a multi-component metamaterial, schematically shown in Fig. 2. The basic principle of operation of this structure is similar to that of multi-lens systems corrected for chromatic aberration. The main difference, however, is the ability of the relatively thin metamaterial “correcting” layer to significantly adjust the dispersion of the much thicker main layer;

Two- and four-layer devices have been fabricated and their dispersion has been analyzed using reflection/transmission measurements, as described in [6-8]. The dispersion of the system is most clearly visualized by the angular position of the Brewster’s angle in the negative refraction regime; the spectral width of the this regime can be assessed by measuring the spectral position of the discontinuity of the Brewster’s angle (beginning of the negative refraction regime) and by abrupt increase of reflection of TE-polarized waves (end of the negative-refraction regime) [6,9,10].

The spectral response of the baseline sample is compared to that of the two- and four-layer structures in Fig.3. Note that the spectrally-corrected structures provide increased bandwidth and significantly flatter response as compared to the single-layer system. Also note that the response of the final

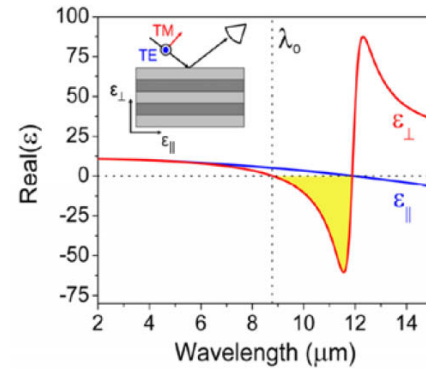


Fig. 1: Dielectric function, ϵ_{\perp} and ϵ_{\parallel} of a n+-i-n+ heterostructure calculated using the effective medium theory and $n_d = 7.5 \times 10^{18} \text{ cm}^{-3}$. The inset shows the layered structure and relative orientation of the dielectric function (ϵ_{\perp} and ϵ_{\parallel}).

fabricated samples closely matches the desired response of theoretically-optimized structure. Quantitatively, operating bandwidth of the sample with n metamaterial (multi)layers, defined as

$$B_n = 2 \frac{\lambda_2 - \lambda_1}{\lambda_2 + \lambda_1} \dots\dots\dots (2)$$

with λ_1 and λ_2 being the limits of the negative refraction region is, yields the following results:

$$B_1 = 26.2\%$$

$$B_2 = 32.0\%$$

$$B_4 = 33.2\%$$

The frequency-corrective coating thus provides the increase of operating bandwidth is 27%; with flat negative refraction regime observed between 8 and 9.5 microns (full negative refraction region spanning 8...11 μm range) [10]. We anticipate that with additional optimization we will be able to further extend the operating range and compensate the material dispersion.

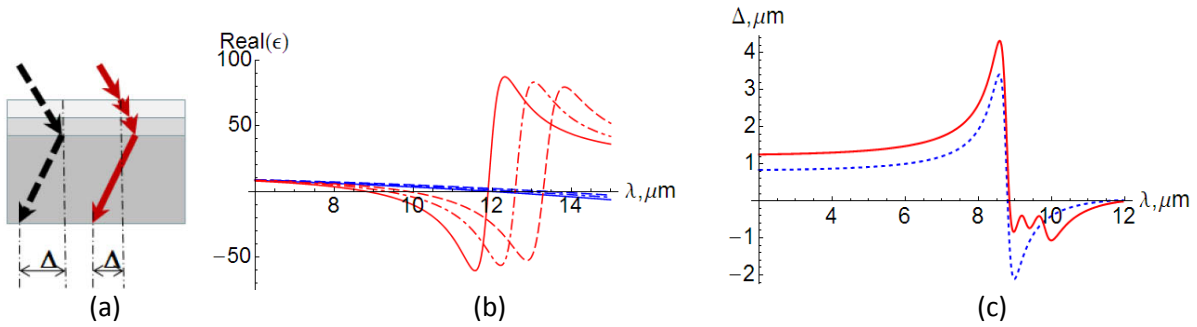


Fig.2 (a) schematic of the multilayerwith dispersion correction; the thin top layers provide compensation for frequency dispersion of the thick bottom layer; (b) dispersion of each individual layer in (a); (c) beam shift due to thick layer in (a) alone (dashed line) and the combined beam shift in the dispersion-compensated system

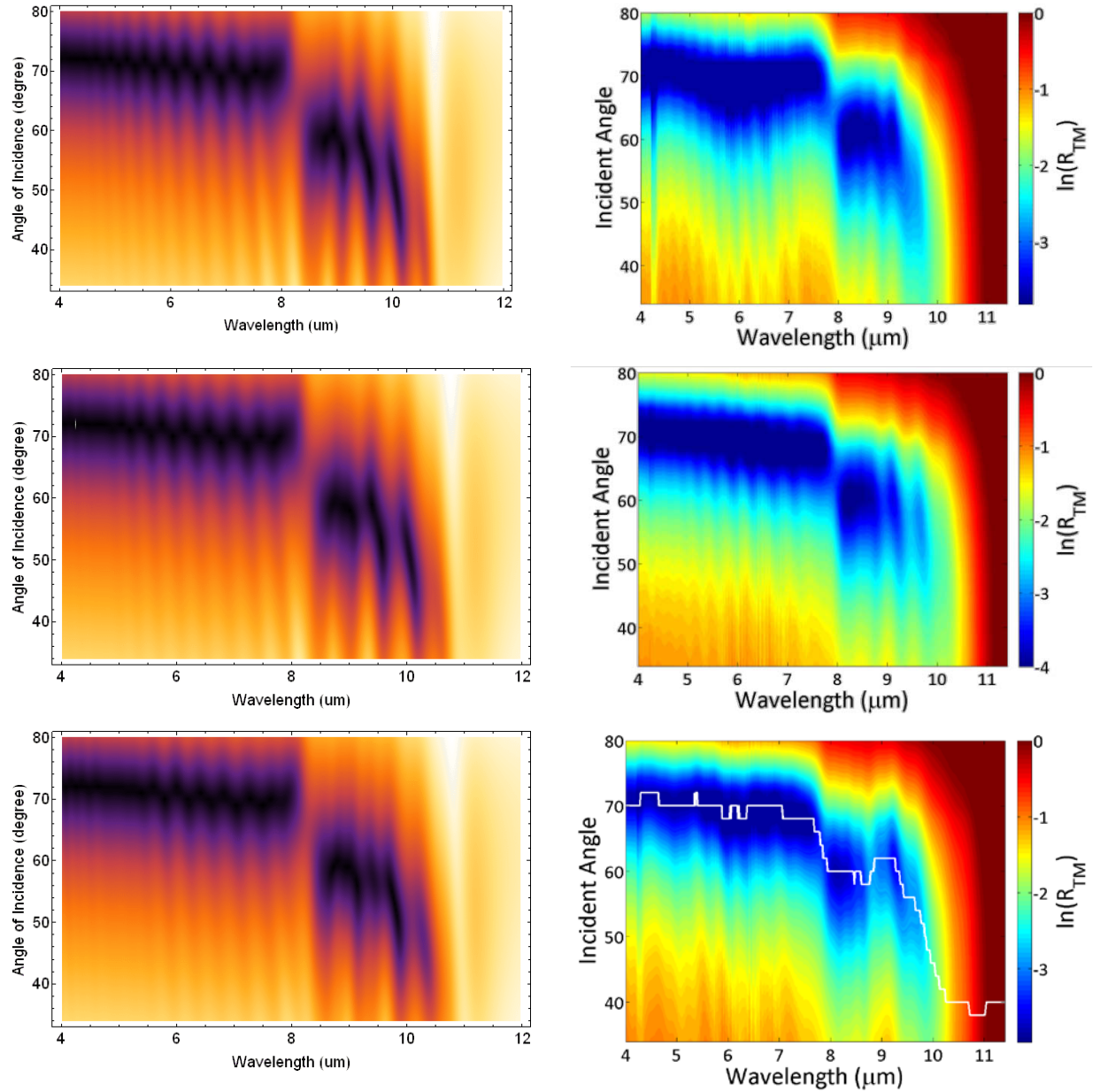


Fig.3. Analytically calculated (left) and experimentally measured (right) dispersion of single-stack MM (top), two-stack system (middle) and four-stack metamaterial (bottom). Frequency dispersion is visualized by frequency/angular dependence of the Brewster's angle, corresponding to the minimum in TM-polarized reflection. Negative refraction region starts from discontinuity of the Brewster angle ($\sim 8\mu m$) and ends when Brewster angle disappears ($\sim 11\mu m$).

Goal 2: loss reduction by incorporating the material gain

As mentioned above, the design of the metamaterial represents a multilayered system of plasmonic (conducting) and dielectric layers. The figure of merit (FOM) of the original metamaterial, defined as the ratio of the real part of refractive index to the imaginary part, varied from 2 to 30 depending on the angle of incidence and wavelength (Fig.4).

The idea of the current thrust of the program was to replace the passive, homogeneous layers of the system with active quantum cascade multistacks, providing electrically-driven optical gain to the device, thereby compensating the losses in the system and increasing FOM, as indicated by the changes in transient transmittance (TT), shown in Fig.5.

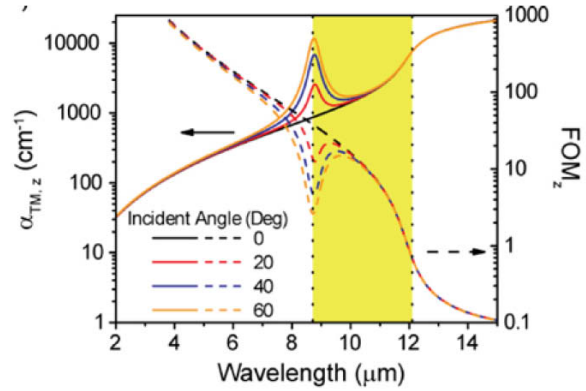


Fig 4. Decay constant α and Figure of Merit (FOM) of a passive semiconductor metamaterial as a function of angle of incidence and frequency

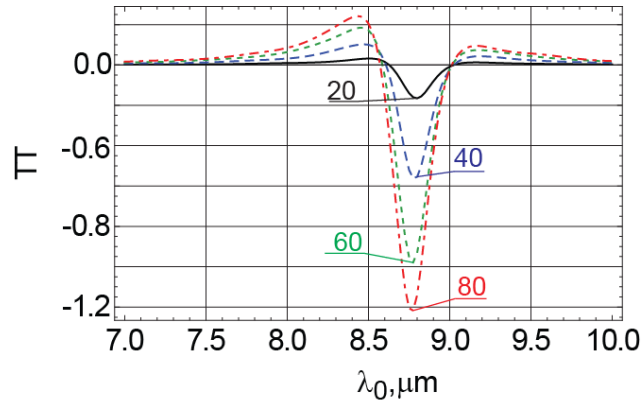


Fig.5 Theoretical calculation of transient transmission as a function of wavelength and incident angle at 10% loss compensation [corresponding to $\sim 100 \text{ cm}^{-1}$ at 20°]

In the course of the project we have fabricated several samples with QC active regions replacing the passive dielectric structures; our first tests of the system suggest that

- The presence of QC regions does not destroy negative refraction response of the system
- The VI characteristics of the device are identical to those of working QC laser (Fig.6)

We are in the process of analyzing the data for second generation of samples, where QC band is spectrally aligned with strong anisotropy to determine the effect of the optical gain on the FOM.

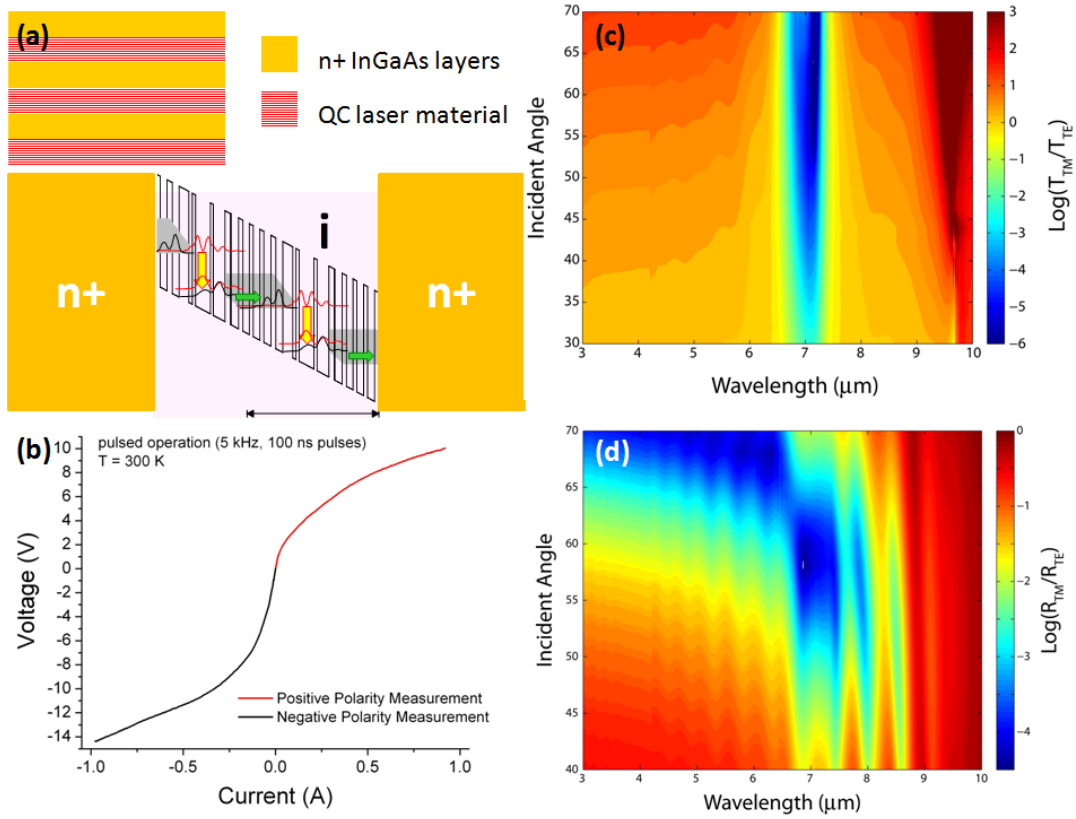


Fig.6 Active metamaterials. (a) schematic design of active metamaterial where intrinsic layers are replaced with QCL structures. (b) IV characteristics of the test sample. The properties are identical to “conventional” QCLs; (c-d) Transmission (c) and reflection (d) spectra of active metamaterials [with no pumping] are similar to those of passive structures

Goal 3: development of planar focusing system with subwavelength focal spots and of a technique to measure the subwavelength objects in the far field

One of the great benefits of strongly anisotropic metamaterials lies in their ability to propagate subwavelength information about the objects into the far-field. This fact is most clearly seen from the dispersion relation for the plane wave that propagates inside anisotropic metamaterial:

$$\frac{k_{\perp}^2}{\epsilon_{\parallel}} + \frac{k_{\parallel}^2}{\epsilon_{\perp}} = \frac{\omega^2}{c^2} \dots\dots\dots (3)$$

where k_{\perp} and k_{\parallel} represent components of the wavevector perpendicular to and parallel to the layers. As seen from the above equation, plane waves carrying subwavelength information, corresponding to $|k_{\parallel}| \gg \omega/c = 2\pi/\lambda_0$, have real values of k_{\perp} , and thus propagate in the anisotropic material. This behavior is in strong contrast to light propagation in conventional (isotropic) media, where the waves with large transverse components of wavevectors must have imaginary component of the wavevector along the direction of propagation, resulting in the exponential decay of these modes (often called evanescent modes).

In this work we utilize strong anisotropy of the metamaterial to develop a planar structure for subwavelength focusing of light. The idea is to deposit a pre-designed diffraction grating on top of the strongly anisotropic medium that would act similar to the well-known Fresnel lens[11] by shaping the intensity profile of incident light and assuring the constructive interference of the portions of incident beam at the pre-defined point in the bulk of metamaterial. Similar to Fresnel lens approach, the grating would break the incident plane wave into a set of Fresnel zones, with the boundaries between neighboring Fresnel zones corresponding to the phase shift of π in the optical phase of the signal. The coordinates of the boundary of the m -th Fresnel zone are given by the relationship:

$$\sqrt{\epsilon_{\parallel} f^2 + \epsilon_{\perp} x_m^2} - \sqrt{\epsilon_{\parallel} f^2 + \epsilon_{\perp} x_0^2} = \pm \frac{m\pi c}{\omega} \dots\dots\dots (4)$$

where x_0 is the coordinate of the first open Fresnel zone, and the sign at the right-hand side of the equation corresponds to the sign of ϵ_{\perp} [12].

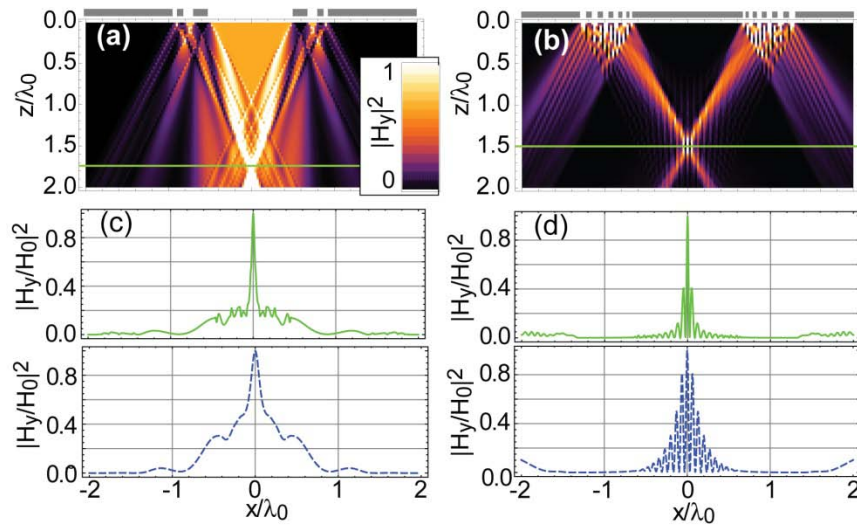


Fig.7 Subwavelength focusing in hypergratings based on planar metamaterials[?]; sizes and positions of the slits are given by Eq.(4); panels (a,b) correspond to low-loss nanowire (a) and nanolayer (c) structures; panels (c,d) show field profiles in focal planes; solid lines: in low-loss systems, dashed lines: full loss structures (see [12] for more details).

The focusing performance of such *hypergrating* is illustrated in Fig.7. It is clearly seen that the device is capable of achieving sub-micron focal spots in the far-field of the grating at LWIR frequency range.

Experimental confirmation of the existence of sub-wavelength focal spots is extremely challenging since no LWIR near-field microscopy currently exists. In order to get around this fundamental problem, we have developed a novel technique for far-field subwavelength imaging. Similar to hypergrating, this technique relies on a diffraction grating, this time deposited at the focal plane of the device (Fig.8). As known from standard diffraction theory[11], the spectrum of the light transmitted through the grating with period Λ will comprise the spectrum of the incident light, combined with the same spectrum shifted by a multiple of Bloch vector $2\pi/\Lambda$. Note that when the period of the grating is smaller than the wavelength, the Bloch shift effectively converts evanescent waves ($|k_{\parallel}| > 2\pi/\lambda_0$) into propagating waves ($|k_{\parallel} - 2\pi m/\Lambda| < 2\pi/\lambda_0$), which in principle enables the detection of subwavelength information in the far field.

The potential problem with this technique, however, lies in the fact that the transmitted signal has the spectra of propagating and evanescent radiation superimposed on top of each other. Similar problem appeared in previous realizations of diffraction grating-based subwavelength imaging [13,14], where the subwavelength information was limited to first Bloch zone ($m = 1$), the far field resolution was of the order of $\lambda_0/4$, and the distinction between the propagating $m = 0$ and evanescent parts of the spectrum was achieved by rotating the polarization of the incident light.

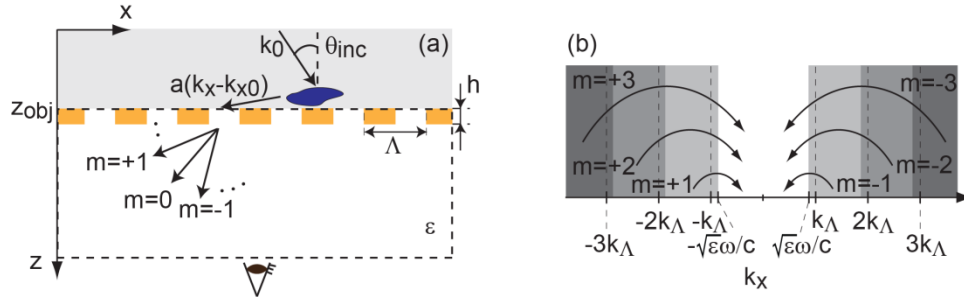


Fig.8 (a) Schematic of the imaging configuration; an object is placed close to the subwavelength plasmonic grating with period Λ and is irradiated by the plane wave with incident angle θ_{inc} ; the far-field intensity is measured inside the material with permittivity ϵ ; (b) transfer of evanescent information into propagating regime by the m -th diffraction order of the grating; normal incidence is assumed

In the case of hypergrating, we need to decompose the information from several Bloch orders, resulting in significant enhancement of far-field resolution ($\sim \lambda_0/20$). To accomplish the above goal, we vary the direction (not polarization) of incident light, measuring the field profile at the given location in the far field of the device as a function of the incident angle. We then compute the transfer function t_m of the diffraction grating that provides the ratio of the amplitude of the m -th Bloch-shifted component behind the grating to the original amplitude of the incident light. Finally, we use nonlinear fit[15] to map the analytically calculated intensity of the signal

$$H_y(x, z, \theta_{inc}) = \left| \sum_m \sum_n w_n a(k_{x,n} - k_{x0}) t_m(k_{x,n} - k_{x0}) \exp(iq_{mn}x) \exp(ik_z(q_{mn})z) \right|^2 \dots (5)$$

to the experimentally measured data. This fitting procedure results in the amplitudes of the incident signal $a(k_x)$ that can be used to reconstruct the image in front of the grating.

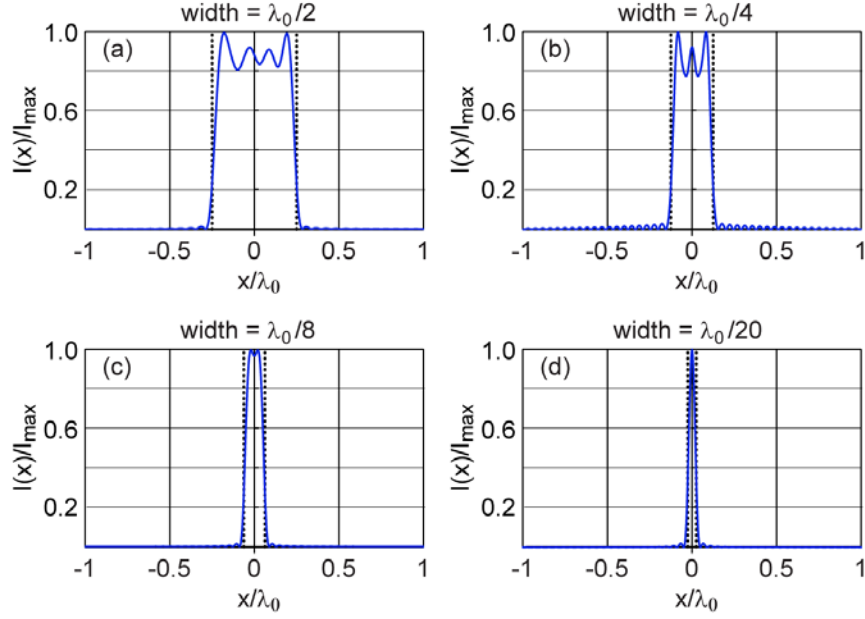


Fig.9 Reconstruction (blue solid curves) of single slits with width (a) $\lambda_0/2$, (b) $\lambda_0/4$, (c) $\lambda_0/8$, and (d) $\lambda_0/20$; black dotted lines represent the object size; vacuum-to-vacuum measurement is assumed

To verify the developed formalism[16], we simulated the far-field intensity distribution, generated by several slits ranging from $\lambda_0/2$ to $\lambda_0/20$, positioned behind the grating with period $\Lambda = 2\lambda_0/3$, used the fitting technique to recover the size of original slit based on these far-field “measurements”. The results of this imaging procedure are illustrated in Fig.9.

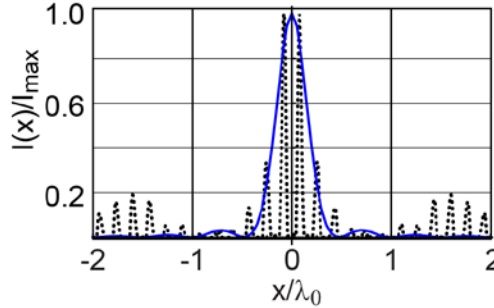


Fig.10 reconstruction of the subwavelength focal spot of the hypergrating shown in Fig.7, based on measurements in vacuum; solid blue and dotted black curves correspond to retrieved and original images respectively

Similar technique can be applied to recover the intensity distribution in the focal spot of the hypergrating. Corresponding simulations are illustrated in Fig.10.

To summarize, we have

- theoretically developed and experimentally demonstrated frequency-dispersion compensation in LWIR metamaterials [10],
- incorporated QC systems into metamaterials with aim to demonstrate first electrically-pumped active metamaterial
- developed theoretical formalism for creation of sub-wavelength focal spots with anisotropic metamaterials [12], and a new technique for subwavelength far-field imaging [16, 17]

Our research revealed a great potential of semiconductor metamaterials for subwavelength imaging and focusing.

References

- [1]. V. G. Veselago, *The electrodynamics of substances with simultaneously negative values of ϵ and μ* , Sov. Phys. Uspekhi **10**, pp. 509-514 (1968);
- [2]. J.B. Pendry "Negative refraction makes a perfect lens" Phys.Rev.Lett, **85**, 3966 (2000); J.B.Pendry and D.R. Smith, *Reversing light with negative refraction*, Physics Today, **57 (6)**, p.37 (2004);
- [3]. V. M. Shalaev, "Optical negative-index metamaterials," Nat. Phot.**1**, 41-48 (2007);
- [4]. N.Fung, H. Lee, C. Sun, X.Zhang, *Sub-diffraction-limited optical imaging with a silver superlens*, Science **308**, 534 (2005); A. Salandrino and N. Engheta, "Far-field subdiffraction optical microscopy using metamaterial crystals: theory and simulations," Phys. Rev. B **74**, 075103 (2006); I.I. Smolyaninov, Y.J. Hung, C.C. Davis, Science **315**, 1699 (2007)
- [5]. A.Alu, N. Engheta, "Light squeezing through arbitrarily shaped plasmonic channels and sharp bends", Phys.Rev.B, **78**, 035440 (2008)
- [6]. A. J. Hoffman, L. Alekseyev, S.S. Howard, K.J. Franz, D. Wasserman, V.A. Podolskiy, E.E. Narimanov, D.L. Sivco, C. Gmachl "Negative refraction in semiconductor metamaterials" – Nature Materials **6**, 946 (2007)
- [7]. A. J. Hoffman, L. Alekseyev, A. Sridhar, P.X. Braun, S. S. Howard, D.L. Sivco, V.A. Podolskiy, E.E. Narimanov, C. Gmachl "Mid-infrared Semiconductor Optical Metamaterials", J. Appl. Phys. **105**, 122411 (2009)
- [8]. A.J. Hoffman, V.A. Podolskiy, D.L. Sivco, C. Gmachl "Sub-diffracted negative and positive index modes in mid-infrared waveguides" - Optics Express **16**, 16404 (2008)
- [9]. V.G. Veselago, E.E. Narimanov, "The left hand of brightness: past, present, and future of negative index materials", Nat. Mat. **5**, 759 (2006)
- [10]. M. Escarra, S. Thongrattanasiri, A. Hoffman, J. Chen, W. Charles, K. Conover, V. Podolskiy, and C. Gmachl, "Broadband, low-dispersion mid-infrared metamaterials", CLEO/QELS proceedings (2010); full manuscript in preparation.
- [11]. M. Born and E. Wolf, "Principles of Optics" (Cambridge U. Press, 1999).
- [12]. S. Thongrattanasiri, V.A. Podolskiy "Hyper-gratings: nanophotonics in planar anisotropic metamaterials", Opt.Lett. **34**, 890 (2009)
- [13]. R. Heintzmann and C. Cremer, SPIE 3568, 185 (1998); M. G. L. Gustafsson, J. Micro. Oxford 198, 82 (2000)
- [14]. S. Durant, Z. W. Liu, J. A. Steele, and X. Zhang, J. Opt. Soc. Am. B **23**, 2383 (2006)
- [15]. W. H. Press, B. P. Flannery, S. A. Teukolsky, and W. T. Vetterling, Numerical Recipes in FORTRAN77 (Cambridge U. Press, 1992)
- [16]. S. Thongrattanasiri, N.A. Kuhta, M.D. Escarra, A.J. Hoffman, C.F. Gmachl, and V.A. Podolskiy, "Analytical technique for subwavelength far field imaging" Proceedings CLEO/QELS 2010.
- [17]. S. Thongrattanasiri, N.A. Kuhta, M.D. Escarra, A.J. Hoffman, C.F. Gmachl, and V.A. Podolskiy, "Analytical technique for subwavelength far field imaging," Applied Physics Letters, Vol. **97**, 101103 (2010). **Applied Physics Letters Top 20 Most Downloaded Article, September 2010.**

Quasi-planar optics: computing light propagation and scattering in planar waveguide arrays

Sukosin Thongrattanasiri, Justin Elser, and Viktor A. Podolskiy*

Department of Physics, 301 Weniger Hall, Oregon State University, Corvallis Oregon 97331, USA

*Corresponding author: viktor.podolskiy@physics.oregonstate.edu

Received August 3, 2009; accepted August 30, 2009;

posted September 16, 2009 (Doc. ID 115087); published October 16, 2009

We analyze wave propagation in coupled planar waveguides, pointing specific attention to modal cross-talk and out-of-plane scattering in quasi-planar photonics. An algorithm capable of accurate numerical computation of wave coupling in arrays of planar structures is developed and illustrated on several examples of plasmonic and volumetric waveguides. An analytical approach to reduce or completely eliminate scattering and modal cross-talk in planar waveguides with anisotropic materials is also presented. © 2009 Optical Society of America

OCIS codes: 050.1755, 160.3918, 240.6690, 230.7390.

1. INTRODUCTION

On-chip communications, surface plasmon optics, and Si photonics are all examples of *planar optics*, where the optical radiation is controllably guided on the plane of a photonic chip. A number of planar optical elements including lenses, mirrors, and on-chip waveguides—both plasmonic and dielectric—have been recently designed, fabricated, and characterized [1–12]. However, with a few exceptions [11,13,14], the majority of recent studies focuses on in-plane propagation of light and neglects out-of-plane scattering of radiation. In this work we analyze the out-of-plane light scattering and modal cross-talk due to effective index change inside planar waveguides and demonstrate that this scattering may substantially affect the propagation of confined modes in complex planar systems. We design a numerical approach to solve the problem of scattering and modal cross-talk in planar or quasi-planar structures that contain anisotropic elements, and present the technique to reduce or completely eliminate the scattering and cross-talk with anisotropic metamaterials [15].

The problem of out-of-plane scattering has been of consistent interest to the photonics community. Although a number of finite-difference and finite-elements techniques, available today, can successfully solve the problem of scattering in relatively small geometries ($\leq 10 \lambda_0$, with λ_0 being free-space wavelength), analysis of wave propagation in an extended system is beyond the capabilities of methods that rely on finite-size meshing of space/time. One of the ways to reduce memory requirements to calculate the field in an extended structure with a moderate number of scattering interfaces is to implement some sort of wave-matching technique where the modal spectrum is constructed to satisfy the solutions of Maxwell's equations in the space, and only boundary conditions at scattering interfaces are enforced, resulting in calculations of *amplitudes* of the modes. Effectively, modal expansion can replace the need to calculate all field components at every *point of space* with the

need to calculate modal amplitudes in every *region of space*.

One of the first descriptions of the wave-matching approach and its applications for highly conductive plasmonic guides can be found in [13,16]. Reference [13] also describes scattering by planar guides with highly symmetric cross-sections. Green's function formalism has been utilized to analyze out-of-plane scattering of plasmonic guides in [17]. An approach to calculate the modal cross-talk and scattering in 1D guides was developed in [18]. Scattering by periodically corrugated systems has been analyzed with rigorous coupled wave analysis (RCWA) in [19]. Recently, the generalization of field expansion to calculate scattering in plasmonic planar guides has been presented in [14]. However, while the mode-matching calculations were proven to be highly efficient, this technique had failed in the proximity to plasmon resonance condition, when the field of a surface wave is highly confined to the proximity of a metal interface. Here we present a wave-matching technique that is capable of solving for wave scattering in complex systems formed by coupled planar waveguides.

The rest of the manuscript is organized as follows. In Section 2, we present the mode structure of an arbitrary planar guide used in this work (Fig. 1). Section 3 is devoted to the development of a mode-matching technique in a quasi-planar system comprising a uniform in *y*-direction array of planar guides. The presented numerical approach is illustrated on examples of light propagation in several plasmonic and metamaterial systems in Section 4. Finally, Section 5 develops the formalism of truly planar photonics where out-of-plane scattering and modal cross-talk are not possible and presents an approach to design extremely low-scattering plasmonic circuits.

Notations. In this work we use the following notations for the electric and magnetic fields in the system: the total electric (*E*) and magnetic (*H*) fields are shown in italic letters; the fields of modal components contributing to the

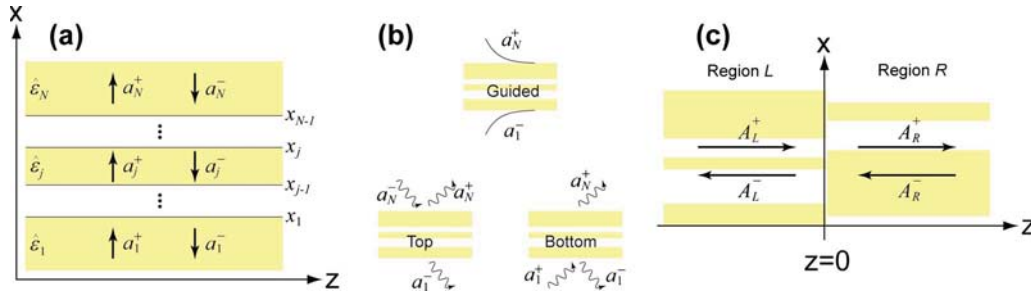


Fig. 1. (Color online) Schematic geometry of the multilayered structures and electromagnetic mode types used in the manuscript. Geometry of the single multilayer stack is shown in (a); panel (b) explains the composition of top, bottom, and guided modes; field profiles in the outside layers of the multilayer are shown; the interface between two multilayer stacks is shown in (c).

total field are represented with symbols \mathbf{E} and \mathbf{H} ; the components of an individual mode in a particular layer of the multilayer stack are represented with calligraphic symbols \mathcal{E} and \mathcal{H} .

2. MODAL SPECTRUM OF PLANAR GUIDES

We start from analysis of a modal spectrum of a planar waveguide, schematically shown in Fig. 1(a). The structure comprises a set of N planar layers with layer interfaces parallel to the yz plane, with the j th layer occupying the space between $x_{j-1} < x \leq x_j$, and having (uniaxial) dielectric permittivity described by a diagonal tensor with

diagonal components $\hat{\epsilon}_j = \{\epsilon_j^{xx}, \epsilon_j^{yy}, \epsilon_j^{zz}\}$. We assume that $x_0 = -\infty$ and $x_N = \infty$. In this section we consider the structure that is infinitely extended in the yz plane.

The electromagnetic fields in this layered system can be represented as a set of transverse-electric (TE) and transverse-magnetic (TM) polarized waves (modes). Each mode of the multilayer constitutes a solution of Maxwell's equations that is finite for $-\infty < x < \infty$ [20]. In a homogeneous layered structure, the mode can be parameterized by a combination of (i) its polarization (TE/TM), (ii) the in-plane components of the wavevector (k_y, k_z), and (iii) a set of layer-specific complex coefficients $\{a_j^\pm\}$ playing the role of amplitudes of the mode components:

$$\vec{\mathbf{E}}(k_y, k_z) = \begin{cases} a_1^+ \vec{\mathcal{E}}_1(k_{x;1}(k_y, k_z), k_y, k_z) + a_1^- \vec{\mathcal{E}}_1(-k_{x;1}(k_y, k_z), k_y, k_z), & x < x_1 \\ \dots & \\ a_j^+ \vec{\mathcal{E}}_j(k_{x;j}(k_y, k_z), k_y, k_z) + a_j^- \vec{\mathcal{E}}_j(-k_{x;j}(k_y, k_z), k_y, k_z), & x_{j-1} < x < x_j \\ \dots & \\ a_N^+ \vec{\mathcal{E}}_N(k_{x;N}(k_y, k_z), k_y, k_z) + a_N^- \vec{\mathcal{E}}_N(-k_{x;N}(k_y, k_z), k_y, k_z), & x_{N-1} < x \end{cases} \quad (1)$$

$$\vec{\mathbf{H}}(k_y, k_z) = \begin{cases} a_1^+ \vec{\mathcal{H}}_1(k_{x;1}(k_y, k_z), k_y, k_z) + a_1^- \vec{\mathcal{H}}_1(-k_{x;1}(k_y, k_z), k_y, k_z), & x < x_1 \\ \dots & \\ a_j^+ \vec{\mathcal{H}}_j(k_{x;j}(k_y, k_z), k_y, k_z) + a_j^- \vec{\mathcal{H}}_j(-k_{x;j}(k_y, k_z), k_y, k_z), & x_{j-1} < x < x_j \\ \dots & \\ a_N^+ \vec{\mathcal{H}}_N(k_{x;N}(k_y, k_z), k_y, k_z) + a_N^- \vec{\mathcal{H}}_N(-k_{x;N}(k_y, k_z), k_y, k_z), & x_{N-1} < x \end{cases} \quad (2)$$

where the fields and dispersion relations in each layer are described by

$$\text{TE - polarized waves: } \begin{cases} \vec{\mathcal{E}}_j = \frac{e^{-i\omega t + i\vec{k} \cdot \vec{r}}}{\sqrt{k_y^2 + k_z^2}} & \{0, \quad k_z, \quad -k_y\} \\ \vec{\mathcal{H}}_j = \frac{e^{-i\omega t + i\vec{k} \cdot \vec{r}} c}{\omega \sqrt{k_y^2 + k_z^2}} & \{-(k_y^2 + k_z^2), \quad k_{x;j} k_y, \quad k_{x;j} k_z\} \\ \frac{k_{x;j}^2 + k_y^2 + k_z^2}{\epsilon_j^{yz}} = \frac{\omega^2}{c^2} \end{cases} \quad (3)$$

$$\text{TM-polarized waves: } \begin{cases} \tilde{\mathcal{E}}_j = \frac{e^{-i\omega t + i\vec{k} \cdot \vec{r}}}{k_y^2 + k_z^2} \\ \tilde{\mathcal{H}}_j = \frac{e^{-i\omega t + i\vec{k} \cdot \vec{r}} \omega}{(k_y^2 + k_z^2)c} \\ \frac{k_{xj}^2}{\varepsilon_j^{yz}} + \frac{k_y^2 + k_z^2}{\varepsilon_j^{xx}} = \frac{\omega^2}{c^2} \end{cases} \quad \left\{ \begin{array}{l} k_y^2 + k_z^2, \quad -\frac{\varepsilon_j^{xx} k_{xj} k_y}{\varepsilon_j^{yz}}, \quad -\frac{\varepsilon_j^{xx} k_{xj} k_z}{\varepsilon_j^{yz}} \\ \{0, \quad \varepsilon_j^{xx} k_z, \quad -\varepsilon_j^{xx} k_y\} \end{array} \right\} \quad (4)$$

Note that for a given mode only two of the amplitudes a_j^\pm are independent of each other. Indeed, the remaining amplitudes can be calculated using the well-known *transfer matrix* method [20]:

$$\begin{pmatrix} a_{j+1}^- \\ a_{j+1}^+ \end{pmatrix} = \alpha_j \begin{bmatrix} (1+K_j)\varphi_j^- & (1-K_j)\varphi_j^+ \\ (1-K_j)/\varphi_j^+ & (1+K_j)/\varphi_j^- \end{bmatrix} \begin{pmatrix} a_j^- \\ a_j^+ \end{pmatrix}, \quad (5)$$

with polarization-dependent parameters φ_j , α_j , and K_j given by $\varphi_j^\pm = \exp[i(k_{xj+1} \pm k_{xj})x_j]$, $\alpha_j^{\text{TE}} = 1/2$, $\alpha_j^{\text{TM}} = \varepsilon_j^{xx}/(2\varepsilon_{j+1}^{xx})$, $K_j^{\text{TE}} = k_{xj}/k_{xj+1}$, $K_j^{\text{TM}} = k_{xj}\varepsilon_{j+1}^{yz}/(k_{xj+1}\varepsilon_j^{yz})$.

For multilayer systems, layer-specific transfer matrices can be multiplied together, yielding the transfer-matrix relating the fields in any two layers of the multilayer stack, and thus solving the problem of reflection and transmission of a plane wave by the multilayer composite. The singular solution that corresponds to nonzero scattered waves on both sides of the multilayer structure ($a_1^-, a_N^+ \neq 0$) with zero incident fields ($a_1^+ = a_N^- = 0$) corresponds to the eigen (guided) mode of the stack [20].

For each polarization, full spectrum of modes supported by the stack includes three groups of waves [see Fig. 1(b)]. The first group contains a discrete spectrum of guided modes, exponentially decaying into first and last layers ($a_1^+ = a_N^- = 0$, $a_1^- = 1$). Here we characterize these waves by the in-plane components of their wavevectors $\{k_y, k_z\}$.

The remaining groups of modes contain the continuum of waves, known as open-waveguide modes [13,14] (bulk modes). The first of these groups represents the modes originated by a plane wave that is incident on the layered structure from the top layer ($a_1^+ = 0$, $a_N^- = 1$), while the second group represents the wave incident on the structure from the bottom layer ($a_1^+ = 1$, $a_N^- = 0$). Here, the modes of the first group ("top modes") are parameterized by the real-valued $k_{x;N}$ in the top (N^{th}) layer, while the "bottom modes" are parameterized by the real-valued $k_{x;1}$ in the bottom (1st) layer.

In the limit of symmetric distribution of permittivity $\hat{\varepsilon}(x) = \hat{\varepsilon}(-x)$, the spectrum of top and bottom modes proposed here is equivalent to the earlier proposed [13] combinations of "standing wave" modes with symmetric and antisymmetric x -profiles. However, in contrast to the latter, the combination of top and bottom modes is more easily generalizable to the case of nonsymmetric (such as plasmonic) planar guides. Note that in a majority of previous studies of plasmonic structures [14], bottom modes were explicitly omitted. As explained below, this omission becomes crucial in the regime of strong surface plasmon

polariton (SPP) scattering, e.g., in proximity to SPP resonance or in plasmonic step geometry (Fig. 3).

Overall, the field inside the guiding structure can be written as

$$\begin{aligned} \vec{E} &= \sum_q [A^{(q)+} \vec{E}(k_y, k_z^{(q)}) + A^{(q)-} \vec{E}(k_y, -k_z^{(q)})] \\ &+ \int_0^\infty [A^{\text{top}+}(k_x) \vec{E}(k_y, k_z(k_{x;N})) + A^{\text{top}-}(k_x) \vec{E}(k_y, -k_z(k_{x;N})) \\ &+ A^{\text{btm}+}(k_x) \vec{E}(k_y, k_z(k_{x;1})) + A^{\text{btm}-}(k_x) \vec{E}(k_y, -k_z(k_{x;1}))] dk_x, \\ \vec{H} &= \sum_q [A^{(q)+} \vec{H}(k_y, k_z^{(q)}) + A^{(q)-} \vec{H}(k_y, -k_z^{(q)})] \\ &+ \int_0^\infty [A^{\text{top}+}(k_x) \vec{H}(k_y, k_z(k_{x;N})) + A^{\text{top}-}(k_x) \vec{H}(k_y, -k_z(k_{x;N})) \\ &+ A^{\text{btm}+}(k_x) \vec{H}(k_y, k_z(k_{x;1})) \\ &+ A^{\text{btm}-}(k_x) \vec{H}(k_y, -k_z(k_{x;1}))] dk_x. \end{aligned} \quad (6)$$

Here we assume that all the modes in the layered material have the same value of k_y . This assumption does not limit the applicability of the developed technique, since due to translational symmetry, any solution of Maxwell's equations in the set of coupled waveguides can be represented as a linear combination of solutions corresponding to a set of k_y values. Likewise, we assume that excitation and response of the system are monochromatic [$E, H \propto \exp(-i\omega t)$]. The linearity of Maxwell's equations makes it possible to generalize the developed formalism for the arbitrary pulse excitation by representing the incident radiation by linear combination of monochromatic waves.

Note that in the process of calculating the waveguide modes, it may be necessary to determine the proper sign of the k_x (or k_z) component of the wavevector in a particular layer. If the component of the wavevector has complex value, this sign is determined from the requirement for the mode to be finite in its domain. If the wavevector component is real, its sign should be determined to impose the propagation of energy in the positive x (or z) direction [21].

The set of waveguide modes defined above allows the introduction of the scalar product

$$\langle \vec{E}_1 | \vec{H}_2^\dagger \rangle = \int_{-\infty}^{\infty} (\vec{E}_1 \times \vec{H}_2^\dagger) \cdot \hat{z} dx, \quad (7)$$

where the dagger (\dagger) corresponds to the adjointed field, i.e., field of the mode propagating in the reversed z direction

[13,18]. It can be shown [13,14,18] that in a given multilayer (i) all TM-polarized waves are orthogonal to all TE-polarized waves, (ii) the guided modes are orthogonal to each other, and (iii) the top and bottom modes may have some coupling, depending on $\hat{\epsilon}_1$ and $\hat{\epsilon}_N$: if $\hat{\epsilon}_1 = \hat{\epsilon}_N$, the top and bottom modes corresponding to the same value of k_x are coupled to each other and are orthogonal to all other modes; if one of the two materials is lossy (as is usually the case with plasmonic structures), the top and bottom modes are, as a rule, orthogonal to each other.

Note that, similar to what has been suggested in [14], the scalar product can be calculated analytically, significantly speeding up the calculation.

3. MODE COUPLING ACROSS MULTILAYER STACKS

A. General Formalism

We now turn to the main point of this work—discussion of coupling of the modes at the boundary between the two multilayer structures. For simplicity, we present results for the case when the interface is located at $z=0$ [Fig. 1(c)]. Generalization of the technique for other locations of the interface is straightforward.

We are solving the classical scattering problem: finding the fields scattered by the interface provided that the incident fields are known. The incident fields are represented by the modes propagating in the $+z$ direction on the left-hand side of the interface ($z < 0$) and by the modes travelling in the $-z$ direction on the right-hand side of the interface ($z > 0$); the scattered fields are represented by the modes travelling in the $-z$ direction on the left-hand side of the interface and by the modes travelling in the $+z$ direction on the right-hand side of the interface. The modal representation [Eqs. (6)] reduces the scattering problem to an arithmetic task of finding the coefficients A_L^- and A_R^+ as a function of A_L^+ and A_R^- , which can be solved by imposing the following set of boundary conditions:

$$\begin{aligned} E_{L_x} &= E_{R_x}; & H_{L_y} &= H_{R_y}, \\ E_{L_y} &= E_{R_y}; & H_{L_x} &= H_{R_x}. \end{aligned} \quad (8)$$

As can be explicitly verified, the remaining boundary conditions follow from Eqs. (8).

In the case of normal incidence ($k_y=0$), TM- and TE-modes do not couple to each other. Correspondingly, in this case the first two boundary conditions in Eqs. (8) describe the reflection, transmission, and scattering of TM-polarized waves, while the remaining two conditions describe the optical properties of TE-polarized modes.

In order to solve the scattering problem, Eqs. (8) need to be converted into the set of coupled linear equations for the amplitudes of the scattered modes. To achieve this goal, we substitute the modal expansion [Eqs. (6)] in Eqs. (8), and subsequently multiply the resulting expressions by the adjointed fields of left- and right-hand side modes, as illustrated below.

B. Numerical Implementation of the Algorithm

In numerical simulations, it is necessary to replace the continuous integration over k_x with finite sums. Thus, Eqs. (6) becomes

$$\begin{aligned} \vec{E} &= \sum_m [A^{(m)+} \vec{E}^{(m)+} + A^{(m)-} \vec{E}^{(m)-}] w^{(m)}, \\ \vec{H} &= \sum_m [A^{(m)+} \vec{H}^{(m)+} + A^{(m)-} \vec{H}^{(m)-}] w^{(m)}, \end{aligned} \quad (9)$$

where $\vec{E}^{(m)\pm} \equiv \vec{E}(k_y, \pm k_z^{(m)})$, and similar for \vec{H} ; the summation in Eqs. (9) goes over all modes (guided, top, and bottom), and the weight factors w are equal to 1 for the guided modes, and are determined by the integration method used for top and bottom modes [22]. Note that the number of modes on the left-hand side of the interface does not necessarily equal to the number of modes on the right-hand side of the interface.

Equations (8) now become

$$\begin{aligned} &\sum_{m=1}^{N_L} [A_L^{(m)+} E_{L_x}^{(m)+} + A_L^{(m)-} E_{L_x}^{(m)-}] w_L^{(m)} \\ &= \sum_{m=1}^{N_R} [A_R^{(m)+} E_{R_x}^{(m)+} + A_R^{(m)-} E_{R_x}^{(m)-}] w_R^{(m)}, \\ &\sum_{m=1}^{N_L} [A_L^{(m)+} H_{L_y}^{(m)+} + A_L^{(m)-} H_{L_y}^{(m)-}] w_L^{(m)} \\ &= \sum_{m=1}^{N_R} [A_R^{(m)+} H_{R_y}^{(m)+} + A_R^{(m)-} H_{R_y}^{(m)-}] w_R^{(m)}, \\ &\sum_{m=1}^{N_L} [A_L^{(m)+} E_{L_y}^{(m)+} + A_L^{(m)-} E_{L_y}^{(m)-}] w_L^{(m)} \\ &= \sum_{m=1}^{N_R} [A_R^{(m)+} E_{R_y}^{(m)+} + A_R^{(m)-} E_{R_y}^{(m)-}] w_R^{(m)}, \\ &\sum_{m=1}^{N_L} [A_L^{(m)+} H_{L_x}^{(m)+} + A_L^{(m)-} H_{L_x}^{(m)-}] w_L^{(m)} \\ &= \sum_{m=1}^{N_R} [A_R^{(m)+} H_{R_x}^{(m)+} + A_R^{(m)-} H_{R_x}^{(m)-}] w_R^{(m)}. \end{aligned} \quad (10)$$

To solve for $N_R + N_L$ unknown amplitudes, we multiply first two equations in Eqs. (10) by the fields of TM-polarized modes and integrate the resulting products over x ; similarly, we multiply the two latter equations by the fields of TE-polarized modes and perform the integration. Assuming that the index m first spans the TE-polarized and then TM-polarized waves, the procedure results in the following two sets of matrix equations:

$$\begin{aligned} \widehat{\mathcal{E}}_{\mathcal{RL}}^{+mn} A_L^{(m)+} + \widehat{\mathcal{E}}_{\mathcal{RL}}^{-mn} A_L^{(m)-} &= \widehat{\mathcal{E}}_{\mathcal{RR}}^{+mn} A_R^{(m)+} + \widehat{\mathcal{E}}_{\mathcal{RR}}^{-mn} A_R^{(m)-}, \\ \widehat{\mathcal{H}}_{\mathcal{RL}}^{+mn} A_L^{(m)+} + \widehat{\mathcal{H}}_{\mathcal{RL}}^{-mn} A_L^{(m)-} &= \widehat{\mathcal{H}}_{\mathcal{RR}}^{+mn} A_R^{(m)+} + \widehat{\mathcal{H}}_{\mathcal{RR}}^{-mn} A_R^{(m)-}, \end{aligned} \quad (11)$$

and

$$\begin{aligned}\widehat{\mathfrak{E}}_{\mathfrak{L}}^{+mn} A_L^{(m)+} + \widehat{\mathfrak{E}}_{\mathfrak{L}}^{-mn} A_L^{(m)-} &= \widehat{\mathfrak{E}}_{\mathfrak{R}}^{+mn} A_R^{(m)+} + \widehat{\mathfrak{E}}_{\mathfrak{R}}^{-mn} A_R^{(m)-}, \\ \widehat{\mathfrak{H}}_{\mathfrak{L}}^{+mn} A_L^{(m)+} + \widehat{\mathfrak{H}}_{\mathfrak{L}}^{-mn} A_L^{(m)-} &= \widehat{\mathfrak{H}}_{\mathfrak{R}}^{+mn} A_R^{(m)+} + \widehat{\mathfrak{H}}_{\mathfrak{R}}^{-mn} A_R^{(m)-},\end{aligned}\quad (12)$$

where the summation over repeated index m is assumed and matrix elements are given by

$$\begin{aligned}\mathfrak{E}_{\mathfrak{R}\{L|R\}}^{\pm mn} &= w_{\{L|R\}}^{(m)} \begin{cases} \int_{-\infty}^{\infty} E_{\{L|R\}_y}^{(m)\pm} H_{R_x}^{(n)-} dx, & n \leq N_R^{\text{TE}} \\ \int_{-\infty}^{\infty} E_{\{L|R\}_x}^{(m)\pm} H_{R_y}^{(n)-} dx, & n > N_R^{\text{TE}} \end{cases}, \\ \mathfrak{H}_{\mathfrak{R}\{L|R\}}^{\pm mn} &= w_{\{L|R\}}^{(m)} \begin{cases} \int_{-\infty}^{\infty} H_{\{L|R\}_x}^{(m)\pm} E_{R_y}^{(n)-} dx, & n \leq N_R^{\text{TE}} \\ \int_{-\infty}^{\infty} H_{\{L|R\}_y}^{(m)\pm} E_{R_x}^{(n)-} dx, & n > N_R^{\text{TE}} \end{cases}, \\ \mathfrak{E}_{\mathfrak{L}\{L|R\}}^{\pm mn} &= w_{\{L|R\}}^{(m)} \begin{cases} \int_{-\infty}^{\infty} E_{\{L|R\}_y}^{(m)\pm} H_{L_x}^{(n)-} dx, & n \leq N_R^{\text{TE}} \\ \int_{-\infty}^{\infty} E_{\{L|R\}_x}^{(m)\pm} H_{L_y}^{(n)-} dx, & n > N_R^{\text{TE}} \end{cases}, \\ \mathfrak{H}_{\mathfrak{L}\{L|R\}}^{\pm mn} &= w_{\{L|R\}}^{(m)} \begin{cases} \int_{-\infty}^{\infty} H_{\{L|R\}_x}^{(m)\pm} E_{L_y}^{(n)-} dx, & n \leq N_R^{\text{TE}} \\ \int_{-\infty}^{\infty} H_{\{L|R\}_y}^{(m)\pm} E_{L_x}^{(n)-} dx, & n > N_R^{\text{TE}} \end{cases}. \quad (13)\end{aligned}$$

Note that the modes of $z < 0$ region are not necessarily orthogonal to the modes in the $z > 0$ region. Thus, the matrices $\widehat{\mathfrak{E}}_{\mathfrak{R}\mathfrak{L}}^{\pm}, \widehat{\mathfrak{H}}_{\mathfrak{R}\mathfrak{L}}^{\pm}, \widehat{\mathfrak{E}}_{\mathfrak{L}\mathfrak{R}}^{\pm}, \widehat{\mathfrak{H}}_{\mathfrak{L}\mathfrak{R}}^{\pm}$ may have substantial nondiagonal components describing cross-talk of the modes across the interface.

In fact, the above matrices are square and invertible only when $N_L = N_R$, in which case one of Eqs. (11) and (12) can provide the information required to solve the scattering problem. However, even in this case, inversion procedure may lead to significant numerical problems and is undesirable. When $N_L \neq N_R$ these matrices are *rectangular* and thus, even theoretically, cannot be inverted. To overcome this difficulty, we reduce Eqs. (11) and (12) to the following set of equations that represent the generalization of transfer-matrix formalism for coupled waveguide structures:

$$\begin{aligned}\begin{cases} \tilde{A}_R^- = \widehat{\mathfrak{R}}_{11} \tilde{A}_L^- + \widehat{\mathfrak{R}}_{12} \tilde{A}_L^+ \\ \tilde{A}_R^+ = \widehat{\mathfrak{R}}_{21} \tilde{A}_L^- + \widehat{\mathfrak{R}}_{22} \tilde{A}_L^+ \end{cases}, \\ \begin{cases} \tilde{A}_L^- = \widehat{\mathfrak{L}}_{11} \tilde{A}_R^- + \widehat{\mathfrak{L}}_{12} \tilde{A}_R^+ \\ \tilde{A}_L^+ = \widehat{\mathfrak{L}}_{21} \tilde{A}_R^- + \widehat{\mathfrak{L}}_{22} \tilde{A}_R^+ \end{cases},\end{aligned}\quad (14)$$

where $\tilde{A}_{\{L|R\}}^{\pm} = \{A_{\{L|R\}}^{(1)\pm}, \dots, A_{\{L|R\}}^{(N_{\{L|R\}})\pm}\}$ and

$$\begin{cases} \mathfrak{R}_{11} = [\widehat{\mathfrak{E}}_{\mathfrak{R}\mathfrak{R}}^{-1} \widehat{\mathfrak{E}}_{\mathfrak{R}\mathfrak{L}} - \widehat{\mathfrak{H}}_{\mathfrak{R}\mathfrak{R}}^{-1} \widehat{\mathfrak{H}}_{\mathfrak{R}\mathfrak{L}}]^{-1} (\widehat{\mathfrak{E}}_{\mathfrak{R}\mathfrak{R}}^{-1} \widehat{\mathfrak{E}}_{\mathfrak{R}\mathfrak{L}} - \widehat{\mathfrak{H}}_{\mathfrak{R}\mathfrak{R}}^{-1} \widehat{\mathfrak{H}}_{\mathfrak{R}\mathfrak{L}}) \\ \mathfrak{R}_{12} = [\widehat{\mathfrak{E}}_{\mathfrak{R}\mathfrak{R}}^{-1} \widehat{\mathfrak{E}}_{\mathfrak{R}\mathfrak{L}} - \widehat{\mathfrak{H}}_{\mathfrak{R}\mathfrak{R}}^{-1} \widehat{\mathfrak{H}}_{\mathfrak{R}\mathfrak{L}}]^{-1} (\widehat{\mathfrak{E}}_{\mathfrak{R}\mathfrak{R}}^{-1} \widehat{\mathfrak{E}}_{\mathfrak{R}\mathfrak{L}} - \widehat{\mathfrak{H}}_{\mathfrak{R}\mathfrak{R}}^{-1} \widehat{\mathfrak{H}}_{\mathfrak{R}\mathfrak{L}}) \\ \mathfrak{R}_{21} = [\widehat{\mathfrak{E}}_{\mathfrak{R}\mathfrak{R}}^{-1} \widehat{\mathfrak{E}}_{\mathfrak{R}\mathfrak{L}} - \widehat{\mathfrak{H}}_{\mathfrak{R}\mathfrak{R}}^{-1} \widehat{\mathfrak{H}}_{\mathfrak{R}\mathfrak{L}}]^{-1} (\widehat{\mathfrak{E}}_{\mathfrak{R}\mathfrak{R}}^{-1} \widehat{\mathfrak{E}}_{\mathfrak{R}\mathfrak{L}} - \widehat{\mathfrak{H}}_{\mathfrak{R}\mathfrak{R}}^{-1} \widehat{\mathfrak{H}}_{\mathfrak{R}\mathfrak{L}}) \\ \mathfrak{R}_{22} = [\widehat{\mathfrak{E}}_{\mathfrak{R}\mathfrak{R}}^{-1} \widehat{\mathfrak{E}}_{\mathfrak{R}\mathfrak{L}} - \widehat{\mathfrak{H}}_{\mathfrak{R}\mathfrak{R}}^{-1} \widehat{\mathfrak{H}}_{\mathfrak{R}\mathfrak{L}}]^{-1} (\widehat{\mathfrak{E}}_{\mathfrak{R}\mathfrak{R}}^{-1} \widehat{\mathfrak{E}}_{\mathfrak{R}\mathfrak{L}} - \widehat{\mathfrak{H}}_{\mathfrak{R}\mathfrak{R}}^{-1} \widehat{\mathfrak{H}}_{\mathfrak{R}\mathfrak{L}}) \end{cases}, \quad (15)$$

$$\begin{cases} \mathfrak{L}_{11} = [\widehat{\mathfrak{E}}_{\mathfrak{L}\mathfrak{L}}^{-1} \widehat{\mathfrak{E}}_{\mathfrak{L}\mathfrak{R}} - \widehat{\mathfrak{H}}_{\mathfrak{L}\mathfrak{L}}^{-1} \widehat{\mathfrak{H}}_{\mathfrak{L}\mathfrak{R}}]^{-1} (\widehat{\mathfrak{E}}_{\mathfrak{L}\mathfrak{L}}^{-1} \widehat{\mathfrak{E}}_{\mathfrak{L}\mathfrak{R}} - \widehat{\mathfrak{H}}_{\mathfrak{L}\mathfrak{L}}^{-1} \widehat{\mathfrak{H}}_{\mathfrak{L}\mathfrak{R}}) \\ \mathfrak{L}_{12} = [\widehat{\mathfrak{E}}_{\mathfrak{L}\mathfrak{L}}^{-1} \widehat{\mathfrak{E}}_{\mathfrak{L}\mathfrak{R}} - \widehat{\mathfrak{H}}_{\mathfrak{L}\mathfrak{L}}^{-1} \widehat{\mathfrak{H}}_{\mathfrak{L}\mathfrak{R}}]^{-1} (\widehat{\mathfrak{E}}_{\mathfrak{L}\mathfrak{L}}^{-1} \widehat{\mathfrak{E}}_{\mathfrak{L}\mathfrak{R}} - \widehat{\mathfrak{H}}_{\mathfrak{L}\mathfrak{L}}^{-1} \widehat{\mathfrak{H}}_{\mathfrak{L}\mathfrak{R}}) \\ \mathfrak{L}_{21} = [\widehat{\mathfrak{E}}_{\mathfrak{L}\mathfrak{L}}^{-1} \widehat{\mathfrak{E}}_{\mathfrak{L}\mathfrak{R}} - \widehat{\mathfrak{H}}_{\mathfrak{L}\mathfrak{L}}^{-1} \widehat{\mathfrak{H}}_{\mathfrak{L}\mathfrak{R}}]^{-1} (\widehat{\mathfrak{E}}_{\mathfrak{L}\mathfrak{L}}^{-1} \widehat{\mathfrak{E}}_{\mathfrak{L}\mathfrak{R}} - \widehat{\mathfrak{H}}_{\mathfrak{L}\mathfrak{L}}^{-1} \widehat{\mathfrak{H}}_{\mathfrak{L}\mathfrak{R}}) \\ \mathfrak{L}_{22} = [\widehat{\mathfrak{E}}_{\mathfrak{L}\mathfrak{L}}^{-1} \widehat{\mathfrak{E}}_{\mathfrak{L}\mathfrak{R}} - \widehat{\mathfrak{H}}_{\mathfrak{L}\mathfrak{L}}^{-1} \widehat{\mathfrak{H}}_{\mathfrak{L}\mathfrak{R}}]^{-1} (\widehat{\mathfrak{E}}_{\mathfrak{L}\mathfrak{L}}^{-1} \widehat{\mathfrak{E}}_{\mathfrak{L}\mathfrak{R}} - \widehat{\mathfrak{H}}_{\mathfrak{L}\mathfrak{L}}^{-1} \widehat{\mathfrak{H}}_{\mathfrak{L}\mathfrak{R}}) \end{cases}. \quad (16)$$

Finally, we combine Eqs. (14) and arrive to the generalization of the scattering-matrix technique that solves the problem of interlayer coupling:

$$\begin{cases} \tilde{A}_L^- = (\hat{I} - \widehat{\mathfrak{L}}_{12} \widehat{\mathfrak{R}}_{21})^{-1} \widehat{\mathfrak{L}}_{11} & \tilde{A}_R^- = (\hat{I} - \widehat{\mathfrak{L}}_{12} \widehat{\mathfrak{R}}_{21})^{-1} \widehat{\mathfrak{L}}_{12} \widehat{\mathfrak{R}}_{22} \tilde{A}_L^+ \\ \tilde{A}_R^+ = (\hat{I} - \widehat{\mathfrak{R}}_{21} \widehat{\mathfrak{L}}_{12})^{-1} \widehat{\mathfrak{R}}_{21} \widehat{\mathfrak{L}}_{11} & \tilde{A}_R^- = (\hat{I} - \widehat{\mathfrak{R}}_{21} \widehat{\mathfrak{L}}_{12})^{-1} \widehat{\mathfrak{R}}_{22} \tilde{A}_L^+ \end{cases}, \quad (17)$$

with \hat{I} being identity matrices. Equations (17) represent the main result of this work.

Before illustrating the accuracy of the developed approach, we would like to underline its main advantages and disadvantages. The approach is ideal for calculation of light propagation in extended structures with a relatively small number of multilayer segments; the increase in the number of segments results in additional memory use for each given segment and, correspondingly, minimizes the advantages of a wave-matching approach over finite-difference and finite-element schemes.

The developed technique provides an efficient solution of the problem of coupling the multilayers with high index contrast (high optical mode density difference) by implementing a multilayer-dependent number of modes. However, our calculations show that careful design of the spectrum of the open-waveguide modes is necessary when the coupling to and from the highly confined modes is calculated.

For guided modes, the approach allows straightforward calculation of intermode cross-talk by calculating the mode-specific pointing-flux and multiplying it by the amplitude of the given mode squared; similarly, the approach allows for easy calculation of emission directionality, naturally separating the fields produced by guided modes from the fields of open-waveguide modes and separating the fields of the incident waves from the fields of the scattered waves.

4. INTERGUIDE COUPLING IN PLASMONIC AND METAMATERIAL SYSTEMS

We now illustrate the accuracy of the presented approach on several examples of plasmonic and metamaterial systems.

A. Light Emission and Scattering by Single-Mode Waveguide

We first consider light coupling to and from the waveguide. As an example, we use a 600-nm-thick Si waveguide surrounded by air, and calculate the coupling between this system and a homogeneous dielectric at $\lambda_0 = 1.5 \mu\text{m}$; $\epsilon_{\text{Si}} = 12.12$ [23].

To analyze the accuracy of our technique we assume that the system is excited by the TM_2 mode with amplitude of 1, and study the percentage of the reflected light into TM_0 , TM_1 , and TM_2 modes as a function of dielectric permittivity of the homogeneous dielectric [see inset in Fig. 2(a)]. For comparison, we have calculated the same parameters with commercial finite-element-method (FEM) software [24]. The perfect agreement between the results of our technique and FEM simulations is shown in Fig. 2. As expected, even for this relatively simple system, the scattering-matrix approach uses orders-of-magnitude less memory than the FEM model. More importantly, scattering-matrix formalism is easily extendable to the case of multiple guides or multiple interfaces.

The field matching obtained with our technique for $\epsilon_D = 12.12$ are illustrated in Fig. 2(c). Panel (d) of the same figure illustrates the matching obtained in coupling between an air-Si-air guide and an anisotropic hyperbolic metamaterial with $\epsilon_D^{xx} = 3.6 + 0.05i$, $\epsilon_D^{yz} = -12.2 + 1.36i$ [25–36].

B. Light Scattering in Plasmonic Systems

To further analyze the accuracy and limitations of the developed field-matching technique, we have calculated the scattering from the plasmonic analog of the Si guide presented above: a 600-nm-thick plasmonic gap waveguide operating at $\lambda_0 = 0.6 \mu\text{m}$. We assume that cladding of this guide is composed from two gold plates with $\epsilon_{\text{Au}} = -8.94$

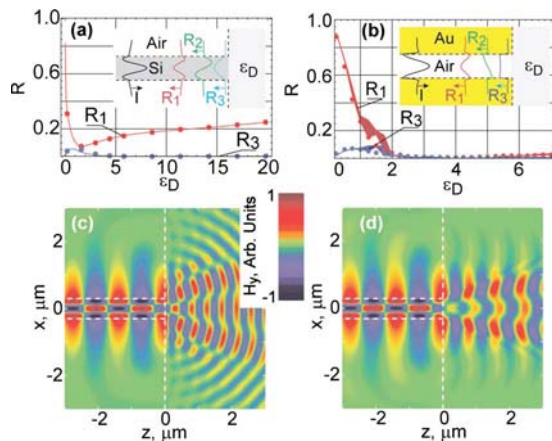


Fig. 2. (Color online) (a) Light reflection in the planar air-Si-air waveguide coupled to a homogeneous dielectric; $\lambda_0 = 1.5 \mu\text{m}$, waveguide thickness $d = 0.6 \mu\text{m}$; the geometry and profiles of the waveguide modes supported by the system are shown in the inset; excitation by TM_2 mode is assumed; the graph shows the comparison between the technique presented here (lines) and FEM simulations (dots); $R_2 = 0$ since the symmetry of TM_1 mode is different from that of TM_0 and TM_2 modes. (b) Reflection in plasmonic gap (Au-Air-Au) waveguide; $\lambda_0 = d = 0.6 \mu\text{m}$; thickness of lines illustrates the convergence of the computations. Panels (c) and (d) illustrate the field distributions in the system (a) with $\epsilon_D = 12.12$ (c) and $\epsilon_D^{xx} = 3.6 + 0.05i$, $\epsilon_D^{yz} = -12.2 + 1.36i$ (d).

+1.32i [23]. The agreement between the mode matching and FEM calculations of modal reflectivity in plasmonic gap guides is shown in Fig. 2(b).

We have further simulated the propagation of plasmonic modes across surface structure defects. In particular, we have used our approach to simulate the SPP propagation in “plasmonic step” geometry (Fig. 3). As expected, when the incoming SPP is travelling on the upper side of the plasmonic step, most of the incident energy is converted into free-space modes. In contrast, when the incident SPP is travelling on the lower side of the step, the majority of energy is converted into the reflected SPP wave.

Our numerical simulations demonstrate that at near-IR frequencies (when $|\epsilon_m| \gg \epsilon_d$), the scattered field can be successfully decomposed into “top” open waveguide modes, as suggested in [14]. However, in the proximity of SPP resonance ($\epsilon_m \approx -\epsilon_d$), the inclusion of the “bottom” modes is necessary to adequately describe the optical properties of the system.

Note that the results of wave-matching simulations are almost identical to those obtained with FEM. Once again, we underline that the wave-matching technique allows for calculation of light propagation in much larger systems than the FEM system does.

To assess the convergence of our method, we have performed a set of simulations for each SPP structure described above, varying the configuration of spectra of top and bottom modes (for simplicity, equidistant k_x spectra between 500 and 3000 modes were used). As expected, our simulations showed that it is necessary to design the spectrum of bulk modes to adequately resolve the SPP propagating at the $z=0$ interface. Interestingly, the “averaged” parameters (such as amplitudes of reflected guided modes) are much more sensitive to spectrum variations than the matching of the boundary conditions at $z=0$ interface, which is often considered to be an indication of accuracy of a numerical method. The typical inter-set varia-

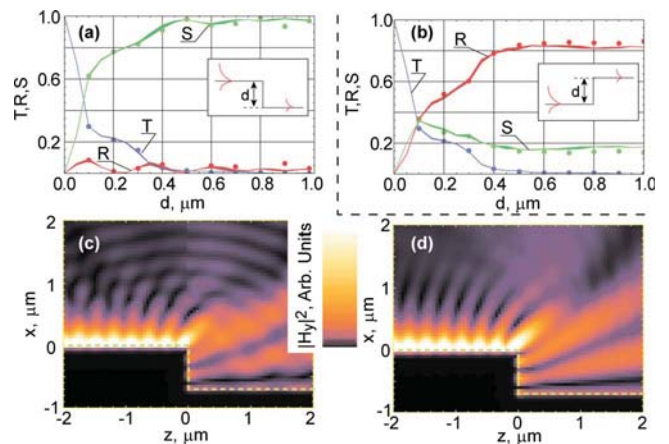


Fig. 3. (Color online) Scattering of the SPP propagating across the Au-Air step; panels (a) and (b) show transmission, reflection, and scattering ($S = 1 - R - T$) of an SPP that is incident on the step; geometry of the structures is shown in insets; lines correspond to the formalism developed in this work (line thickness represents data variation due to changes in spectra of bulk modes); dots represent results from FEM simulations; panels (c) and (d) illustrate the field distributions obtained from scattering-matrix (c) and FEM (d) simulations for $d = 0.7 \mu\text{m}$.

tion of reflection, transmission, and scattering are illustrated in Figs. 2 and 3. The latter figure also shows the agreement between the field distribution obtained with our generalized scattering-matrix formalism and with FEM.

5. TRULY PLANAR OPTICS

We now turn to the analysis of intermode coupling and out-of-mode scattering in planar optics. Planar optics, in general (and SPP optics in particular), are fundamentally different from their free-space counterparts. Thus, when a plane wave is incident on the planar interface, the scattered field can be decomposed into one reflected plane wave and one transmitted plane wave. In contrast to this behavior, when one guided mode is incident on the planar interface between two waveguides, it generates a continuum of open-waveguide modes in addition to the (sets of) reflected and transmitted guided waves.

As seen from Figs. 4 and 5 and from [14], the typical interface between waveguide systems leads to scattering of about 20% of incident radiation. Every attempt to change the effective index of the mode in planar structures is necessarily accompanied by modal cross-talk or by out-of-plane scattering of radiation.

It is possible, however, to utilize anisotropic metamaterials to completely eliminate the cross-talk, and to map the familiar laws of 3D optics to optics of planar guides. The main idea of planar optics lies in the ability to guide light along the planar optical circuit with no out-of-plane scattering or modal cross-talk. In this section we assume that the layers on both sides of the interface are aligned with each other ($x_{Lj}=x_{Rj}$).

In order to realize the efficient control over pulse propagation in the plane, the two layered structures must

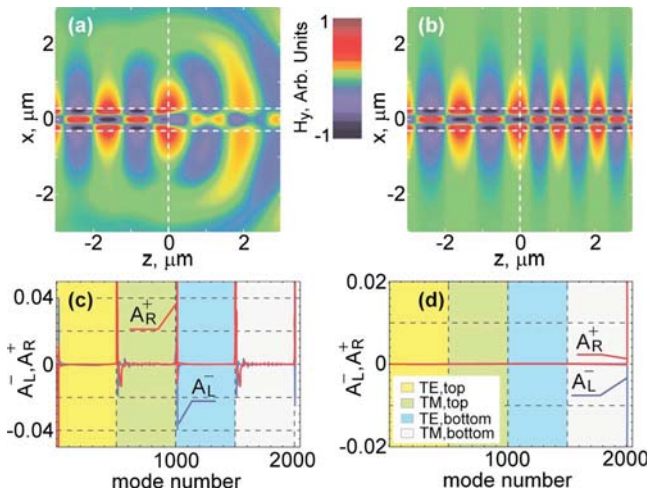


Fig. 4. (Color online) (a,c) An interface between an air-Si-air waveguide and isotropic air ($\epsilon=6.06$)-air guide leads to substantial modal cross-talk, polarization mixing, and out-of-plane scattering; while the interface between air-Si-air waveguide and its anisotropic truly planar optics analog allows for ideal mode matching with light steering capabilities (b,d); guided modes in (c,d) correspond to mode number >2000 ; the system is excited by a TM_2 guided mode propagating at the angle 30° to the $z=0$ interface; the amplitudes of modes in panels (c,d) are normalized to the amplitude of the incident mode.

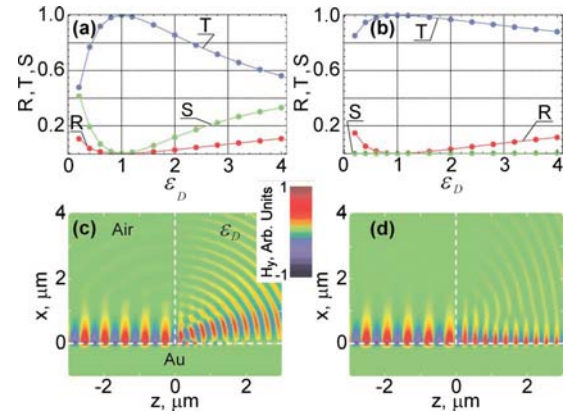


Fig. 5. (Color online) Anisotropic coatings (b, d) can significantly reduce (and almost eliminate) the scattering losses in plasmonic circuits; the figure shows reflection, transmission, and scattering in conventional plasmonic circuit (a) and in a plasmonic system where the space $x>0, z>0$ filled with material $\epsilon_{yz}=1, \epsilon_{xx}=\epsilon_D$ (b); field distribution for $\epsilon_D=4$ (c) clearly shows that only a fraction of incident SPP is transferred into SPP on the right-hand side of the interface; on the other hand, the interface between the anisotropic system with $\epsilon_{yz}=1, \epsilon_{xx}=4$ (d) allows for substantial modulation of SPP index, and results in almost perfect SPP-SPP coupling across a $z=0$ interface.

(i) have the same number of guided modes, and (ii) provide the ability to independently control the index of the mode [crucial for steering the light] and modal profile [crucial for optimizing the overlap integrals involved in $\hat{\epsilon}$ and $\hat{\eta}$ matrices].

As shown in [15] on the example of surface waves, these conditions can be satisfied when

$$\begin{aligned} \epsilon_{Lj}^{yz} &= \epsilon_{Rj}^{yz}, \\ n^2 \epsilon_{Lj}^{xx} &= \epsilon_{Rj}^{xx}, \end{aligned} \quad (18)$$

with n being the constant number that does not depend on layer number j .

As can be explicitly verified, when Eq. (18) is satisfied, all $\hat{\epsilon}$ and $\hat{\eta}$ matrices become diagonal. Thus, the intermode coupling is absent across the interface. The interface remains completely transparent to TE-polarized waves, while reflection and refraction of TM-polarized modes are controlled by the ratio of out-of-plane permittivities. The direction and amplitudes of the reflected and refracted modes are related to the direction and amplitude of the incident modes via the following Snell's law,

$$\sin(\theta_i) = \sin(\theta_r) = n \sin(\theta_t), \quad (19)$$

and Fresnel coefficients,

$$\frac{A_L^{(m)-}}{A_L^{(m)+}} = \frac{k_{L_z}^{(m)} - k_{R_z}^{(m)}}{k_{L_z}^{(m)} + k_{R_z}^{(m)}}, \quad \frac{A_R^{(m)+}}{A_L^{(m)+}} = \frac{2k_{L_z}^{(m)}}{k_{L_z}^{(m)} + k_{R_z}^{(m)}}. \quad (20)$$

The above equations represent generalization of the formalism of Ref. [15] to multilayered guides.

The concept of truly 2D optics is illustrated in Fig. 4 on example of an air-Si-air system coupled to a metamaterials waveguide. As expected, reflection of a single mode in a conventional planar system is accompanied not only

by significant radiation scattering and modal cross-talk but also by cross-polarization coupling. In contrast, for metamaterial guides the single-incident mode excites one reflected wave and one transmitted wave.

Low-Scattering Plasmonics. An interesting extension of truly planar optics is possible in plasmonic systems. From the fabrication standpoint, it is highly desirable that the plasmonic circuit is fabricated on top of common metallic substrate.

Fabrication of an extremely low-scattering plasmonic circuit is possible when using anisotropic dielectrics deposited on noble metals in the limit of visible and near-IR frequencies, where the permittivity of metal is much larger than the permittivity of dielectric ($|\epsilon_m| \gg \epsilon_d^{xx}, \epsilon_d^{yz}$).

Consider the situation where the in-plane (yz) component of permittivity of a dielectric is kept constant across a plasmonic system, and only the out-of-plane (xx) component of permittivity of the superstrate is varied. In such a system the propagation constant of the plasmonic mode, approximately given by [37]

$$k_y^2 + k_z^2 \approx \epsilon_d^{xx} \left(1 + \frac{\epsilon_d^{yz}}{|\epsilon_m|} \right) \frac{\omega^2}{c^2}, \quad (21)$$

can be effectively controlled by changing the parameter ϵ_d^{xx} .

In the same limit, the exponential decay of the mode into the dielectric [$E, H \propto \exp(-\kappa_d x)$, $\kappa_d \approx \omega/c \sqrt{\epsilon_d^{yz}/|\epsilon_m|}$] does not depend on its propagation constant. The only source of out-of-plane scattering in such a structure is related to a weak dependence of the field profile in metal [$E, H \propto \exp(\kappa_m x)$] on ϵ_d^{xx} : $\kappa_m \approx \omega/c \sqrt{|\epsilon_m|(1 - \epsilon_d^{xx}/|\epsilon_m|)}$.

As seen from Fig. 5, anisotropy of dielectric superstrate, achievable, for example, with electrooptic effect [37], provides orders-of-magnitude suppression of out-of-plane scattering in plasmonic systems with respect to isotropic counterparts.

6. CONCLUSIONS

To conclude, we have developed a reliable numerical technique for calculation of light propagation in planar guides and in arrays of planar guides. We have illustrated the developed formalism on examples of photonic, metamaterial, and plasmonic guides, and presented an approach to utilize anisotropic metamaterials for minimization and elimination of modal cross-talk in planar optical circuits.

This work was sponsored by the Office of Naval Research (ONR) (grant No. N00014-07-1-0457), the National Science Foundation (NSF) (grant ECCS-0724763), and the U. S. Air Force Office of Scientific Research (AFOSR) (grant FA9550-09-1-0029).

REFERENCES

1. S. I. Bozhevolnyi, V. S. Volkov, and K. Leosson, "Localization and waveguiding of surface plasmon polaritons in random nanostructures," *Phys. Rev. Lett.* **89**, 186801 (2002).
2. S. A. Maier, P. G. Kik, H. A. Atwater, S. Meltzer, E. Harel, B. E. Koel, and A. A. G. Requicha, "Local detection of electromagnetic energy transport below the diffraction limit in metal nanoparticle plasmon waveguides," *Nature Mater.* **2**, 229–232 (2003).
3. I. I. Smolyaninov, J. Elliot, A. V. Zayats, and C. C. Davis, "Far-field optical microscopy with a nanometer-scale resolution based on the in-plane image magnification by surface plasmon polaritons," *Phys. Rev. Lett.* **94**, 057401 (2005).
4. H. Shin and S. Fan, "All-angle negative refraction for surface plasmon waves using a metal-dielectric-metal structure," *Phys. Rev. Lett.* **96**, 073907 (2006).
5. S. I. Bozhevolnyi, V. S. Volkov, E. Devaux, J. Y. Laluet, and T. W. Ebbesen, "Channel plasmon subwavelength waveguide components including interferometers and ring resonators," *Nature* **440**, 508–511 (2006).
6. A. D. Boardman, *Electromagnetic Surface Modes* (Wiley, 1982).
7. W. L. Barnes, A. Dereux, and T. W. Ebbesen, "Surface plasmon subwavelength optics," *Nature* **424**, 824–830 (2003).
8. M. I. Stockman, "Nanofocusing of optical energy in tapered plasmonic waveguides," *Phys. Rev. Lett.* **93**, 137404 (2004).
9. R. Zia and M. L. Brongersma, "Surface plasmon polariton analogue to Young's double-slit experiment," *Nature Nanotech.* **2**, 426–429 (2007).
10. Z. Liu, J. M. Steele, H. Lee, and X. Zhang, "Tuning the focus of a plasmonic lens by the incident angle," *Appl. Phys. Lett.* **88**, 171108 (2006).
11. I. I. Smolyaninov, D. L. Mazzoni, J. Mait, and C. C. Davis, "Experimental study of surface-plasmon scattering by individual surface defects," *Phys. Rev. B* **56**, 1601–1611 (1997).
12. Y. Vlasov, W. M. J. Green, and F. Xia, "High-throughput silicon nanophotonic wavelength-insensitive switch for on-chip optical networks," *Nat. Photon.* **2**, 242–246 (2008).
13. V. V. Schevchenko, *Continuous Transitions in Open Waveguides* (Golem, 1971).
14. R. F. Oulton, D. F. P. Pile, Y. Liu, and X. Zhang, "Scattering of surface plasmon polaritons at abrupt surface interfaces: implications for nanoscale cavities," *Phys. Rev. B* **76**, 035408 (2007).
15. J. Elser and V. A. Podolskiy, "Scattering-free plasmonic optics with anisotropic metamaterials," *Phys. Rev. Lett.* **100**, 066402 (2008).
16. P. J. B. Clarricoats and K. R. Slinn, "Numerical method for the solution of waveguide-discontinuity problems," *Electron. Lett.* **2**, 226–228 (1966).
17. T. Sondergaard and S. I. Bozhevolnyi, "Out-of-plane scattering properties of long-range surface plasmon polariton gratings," *Phys. Status Solidi B* **242**, 3064–3069 (2005).
18. T. Rozzi and M. Mongiardo, *Open Electromagnetic Waveguides* (Inspec/IEE, 1997).
19. M. G. Moharam and T. K. Gaylord, "Rigorous coupled-wave analysis of planar-grating diffraction," *J. Opt. Soc. Am.* **71**, 811–818 (1981).
20. M. Born and E. Wolf, *Principles of Optics* (Cambridge Univ. Press, 1999).
21. A. A. Govyadinov, V. A. Podolskiy, and M. A. Noginov, "Active metamaterials: sign of refractive index and gain-assisted dispersion management," *Appl. Phys. Lett.* **91**, 191103 (2007).
22. W. H. Press, W. T. Wetterling, S. A. Teukolsky, and B. P. Flannery, *Numerical Recipes in Fortran 77* (Cambridge Univ. Press, 1992).
23. E. Palik, ed., *The Handbook of Optical Constants of Solids* (Academic, 1997).
24. For details see COMSOL Multiphysics User's Guide and RF Module User's Guide; COMSOL (1994–2009); www.comsol.com.
25. V. M. Shalaev, "Optical negative-index metamaterials," *Nat. Photon.* **1**, 41–48 (2007).
26. R. Wangberg, J. Elser, E. E. Narimanov, and V. A. Podolskiy, "Nonmagnetic nanocomposites for optical and infrared negative-refractive-index media," *J. Opt. Soc. Am. B* **23**, 498–505 (2006).
27. J. Yao, Z. Liu, Y. Liu, Y. Wang, C. Sun, G. Bartal, A. M.

- Stacy, and X. Zhang, "Optical negative refraction in bulk metamaterials of nanowires," *Science* **321**, 930 (2008).
28. C. Reinhardt, S. Passinger, B. N. Chichkov, W. Dickson, G. A. Wurtz, P. Evans, R. Pollard, and A. V. Zayats, "Restructuring and modification of metallic nanorod arrays using femtosecond laser direct writing," *Appl. Phys. Lett.* **89**, 231117 (2006).
 29. Y. F. Chen, P. Fischer, and F. W. Wise, "Negative refraction at optical frequencies in nonmagnetic two-component molecular media," *Phys. Rev. Lett.* **95**, 067402 (2005) and Reply **98**, 059702 (2007).
 30. G. Dolling, C. Enkrich, M. Wegener, C. M. Soukoulis, and S. Linden, "Simultaneous negative phase and group velocity of light in a metamaterial," *Science* **312**, 892–894 (2006).
 31. Z. Jacob, L. V. Alekseyev, and E. Narimanov, "Optical hyperlens: far-field imaging beyond the diffraction limit," *Opt. Express* **14**, 8247–8256 (2006).
 32. A. Salandrino and N. Engheta, "Far-field subdiffraction optical microscopy using metamaterial crystals: theory and simulations," *Phys. Rev. B* **74**, 075103 (2006).
 33. Z. Liu, H. Lee, Y. Xiong, C. Sun, and X. Zhang, "Far-field optical hyperlens magnifying sub-diffraction-limited objects," *Science* **315**, 1686 (2007).
 34. I. I. Smolyaninov, Y. J. Huang, and C. C. Davis, "Magnifying superlens in the visible frequency range," *Science* **315**, 1699–1701 (2007).
 35. J. B. Pendry, "Negative refraction makes a perfect lens," *Phys. Rev. Lett.* **85**, 3966–3969 (2000).
 36. S. Thongrattanasiri and V. A. Podolskiy, "Hypergratings: nanophotonics in planar anisotropic metamaterials," *Opt. Lett.* **34**, 890–892 (2009).
 37. V. A. Podolskiy and J. Elser, "Electroplasmonics: dynamical plasmonic circuits with minimized parasitic scattering (QTuJ2)," presented at the Conference on Lasers and Electro-Optics (CLEO) and the International Quantum Electronics Conference (IQEC), Washington, D.C., May 4–8, 2008.

Broadband, Low-Dispersion, Mid-Infrared Metamaterials

Matthew D. Escarra¹, Sukosin Thongrattanasiri², Anthony J. Hoffman¹,
Jianxin Chen^{1,3}, William O. Charles¹, Viktor A. Podolskiy², and Claire Gmachl¹

¹ Department of Electrical Engineering, Princeton University, Princeton, NJ 08544, USA

² Department of Physics, Oregon State University, Corvallis, OR 97331, USA

³ Current address: Shanghai Institute of Technical Physics, Chinese Academy of Sciences, Shanghai 200083, China

Author e-mail address: escarra@princeton.edu

Abstract: Broad-bandwidth, low-dispersion, optical metamaterials are desired. Reflection measurements show that, by using multiple-metamaterial semiconductor stacks of varying thickness and doping, bandwidth is improved by 47% over a single-stack mid-infrared metamaterial, and dispersion appears reduced.

©2010 Optical Society of America

OCIS codes: (160.3918) Metamaterials; (160.4670) Optical materials

1. Introduction

Optical metamaterials exhibiting negative refraction have drawn considerable interest in recent years due to their potential for subwavelength imaging [1] and optical cloaking [2]. More generally, the synthetic nature of these materials provides the potential for significant engineering of their optical response, allowing great creativity in designing new optical materials for a multitude of applications. Recently demonstrated, all-semiconductor, mid-infrared metamaterials show much promise due to their relative low loss, 3-D nature, and straightforward fabrication [3]. However, the spectral bandwidth of negative refraction for a given material and the large dispersion in this negative refraction spectral region currently make these materials unsuitable for applications involving wide-band signals, such as imaging. Here, we demonstrate that these materials can be engineered to produce a broadband, low-dispersion optical response, by forming composite structures of multiple-metamaterial stacks.

2. Material design

The mid-infrared metamaterials used in this study are composed of interleaved 80 nm thick layers of lattice-matched $\text{In}_{0.53}\text{Ga}_{0.47}\text{As}$ and $\text{Al}_{0.48}\text{In}_{0.52}\text{As}$. These layers are grown in a stack by molecular beam epitaxy (MBE) on a low-doped InP substrate. The InGaAs layers are highly doped with Si atoms to create a plasma resonance of free carriers, while the AlInAs layers are left undoped. Conventionally, the InGaAs layers are doped at a uniform level, providing a single-wavelength plasma resonance [3]. In this work, we use multiple doping levels in the same structure, in order to broaden the region of negative refraction and to reduce dispersion in the angle of refraction. This is achieved by growing one metamaterial stack in a conventional manner, followed by growing another stack with different doping directly on top in the same growth chamber, and so forth. By accumulating multiple resonances on top of one another in the same structure, the optical response can be tailored. There are two variables used in designing the behavior of each stack: doping and stack thickness. The doping level determines the critical wavelength, λ_0 , which is the spectral location of the transition from positive to negative refraction. Higher doping leads to a shorter critical wavelength. The thickness of the stack determines the length of interaction with the material.

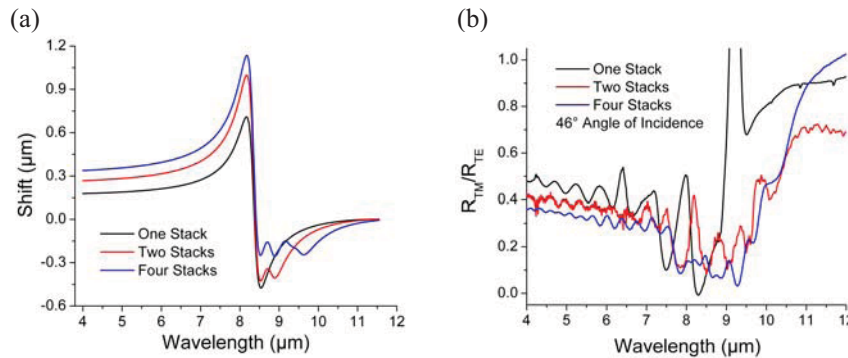


Fig. 1. (a) Calculation of expected lateral (in-plane) shift for light passing through a composite metamaterial consisting of one, two, and four conventional metamaterial stacks. (b) Measured ratio of transverse magnetic/transverse electric reflectance (R_{TM}/R_{TE}) off of the surface of these three different metamaterials at an incidence angle of 46 degrees.

We designed three structures in this study. The first is a baseline single-stack structure consisting of 40 periods of interleaved InGaAs/AlInAs layers grown on InP, with InGaAs layers doped at $10.9 \times 10^{18} \text{ cm}^{-3}$, for a total epitaxial-layer thickness of $6.4 \text{ }\mu\text{m}$. The second sample is a two-stack metamaterial, where the first stack grown on the InP substrate consists of 10 periods ($1.6 \text{ }\mu\text{m}$ thick) with InGaAs doped at $9.0 \times 10^{18} \text{ cm}^{-3}$, and the second stack grown consists of 50 periods ($8 \text{ }\mu\text{m}$ thick) with InGaAs doped at $10.0 \times 10^{18} \text{ cm}^{-3}$. The third sample is a four-stack metamaterial, where the first stack grown on InP contains 6 periods ($0.96 \text{ }\mu\text{m}$ thick) with InGaAs doped at $7.7 \times 10^{18} \text{ cm}^{-3}$, the second contains 7 periods ($1.12 \text{ }\mu\text{m}$ thick) with InGaAs doped at $8.2 \times 10^{18} \text{ cm}^{-3}$, the third contains 13 periods ($2.08 \text{ }\mu\text{m}$ thick) with InGaAs doped at $9.0 \times 10^{18} \text{ cm}^{-3}$, and the fourth contains 50 periods ($8 \text{ }\mu\text{m}$ thick) with InGaAs doped at $10.0 \times 10^{18} \text{ cm}^{-3}$. By using a transfer matrix method to compute the coefficients of full electromagnetic waves propagating through each of the stacks, the beam shift (distance light translates in the plane of the stacks as it passes through the sample) can be calculated versus wavelength, shown in Fig. 1(a). This reveals the expected bandwidth and flatness of the response in the negative refraction (negative shift) region for each structure. From this plot, one can see that the multi-stack metamaterials have broader and flatter negative refraction.

3. Sample characterization

Each of the three grown wafers was characterized through measurements of reflection off of the epitaxial-layer. The measurements were performed with a Fourier-transform infrared spectrometer and its internal source, along with a liquid nitrogen-cooled mercury-cadmium-telluride detector. Reflection measurements were taken versus angle of incidence of the source incident on the sample, with angles ranging from 36° to 80° in 2° increments. A polarizer was used to measure transverse magnetic (TM) and transverse electric (TE) reflection at each angle, all versus wavelength. Spectra were normalized to a background measurement. Incoming TM polarized light experiences negative refraction, whereas TE polarized light does not. A clear discontinuity in the Brewster angle of TM to TE polarized reflection is indicative of this effect. Fig. 1(b) compares spectra at an incidence angle of 46° for all three samples. Furthermore, in Fig. 2, one can see the TM reflection over TE reflection ratio for all angles versus wavelength for each of the three samples: (a) the single-stack material, (b) the two-stack material, and (c) the four-stack material. As we see in these spectra, where the negative refraction region is within dashed lines, the multiple-stack metamaterials have a broader bandwidth of negative refraction. The negative refraction region starts where there is a discontinuity in the Brewster angle ($\lambda_0 \approx 7.6 \text{ }\mu\text{m}$ in Fig. 2(b)) and ends where the TM/TE reflection rises sharply ($R_{\text{TM}}/R_{\text{TE}} = 0.5$); the single-stack has a bandwidth of 21%, the two-stack has a bandwidth of 31%, and the four-stack has a bandwidth of 30%, which is an increase by 47% in relative bandwidth over the single stack. In addition, dispersion appears to be reduced in the negative refraction region for the multiple-stack structures, where the Brewster angle is varying less quickly with wavelength in Figs. 2(b) and 2(c) than it is in Fig 2(a).

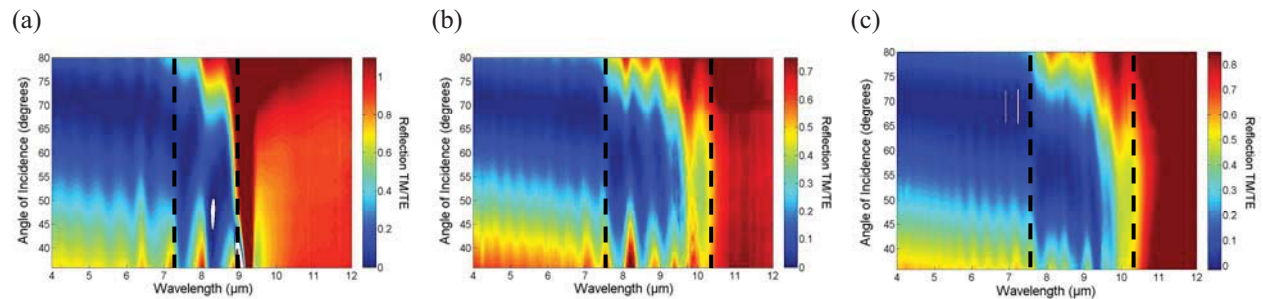


Fig. 2. Ratio of TM over TE surface reflection (color scale) versus angle of incidence and wavelength for (a) a conventional single-stack mid-infrared metamaterial, (b) a broadband metamaterial consisting of two stacks, and (c) a broadband metamaterial consisting of four stacks. The negative refraction region is demarcated by dashed lines.

4. Conclusions

All-semiconductor mid-infrared metamaterials have been demonstrated with enhanced bandwidth and reduced dispersion. Bandwidth was increased from 21% in a conventional reference structure to 31% in a composite structure featuring two metamaterials stacked in succession (a 47% relative increase). Furthermore, dispersion in the negative refraction region appeared reduced in the composite metamaterial. The relatively simple fabrication of these materials allows much potential for creative manipulation of the optical response.

This work is supported in part by AFOSR (grant #FA9550-09-1-0029).

5. References

- [1] Z. Liu, H. Lee, Y. Xiong, C. Sun, and X. Zhang, *Science*, **315**, 1686 (2007).
- [2] J. Valentine, J. Lee, T. Zentgraf, G. Bartal, and X. Zhang, *Nature Mater.*, **8**, 568-571 (2009).
- [3] A.J. Hoffman, L. Alekseyev, S.S. Howard, K.J. Franz, D. Wasserman, V.A. Podolskiy, E.E. Narimanov, D.L. Sivco, and C. Gmachl, *Nature Mater.* **6**, 946-950 (2007).

Analytical technique for determining the size of subwavelength focal spots in far field

Sukosin Thongrattanasiri¹, Anthony J. Hoffman², Matthew Escarra², Claire F. Gmachl², and Viktor A. Podolskiy^{1,3,*}

¹Department of Physics, Oregon State University, 301 Weniger Hall, Corvallis, OR 97331, USA

²Department of Electrical Engineering, Princeton University, Engineering Quadrangle, Olden Street, Princeton, NJ 08544, USA

³Department of Physics and Applied Physics, University of Massachusetts Lowell, One University Avenue, Lowell, MA 01854, USA

*viktor_podolskiy@uml.edu

Abstract: We develop a technique for determining the size of subwavelength focal spots without near-field microscopy, based on carefully designed gratings that convert the subwavelength information into propagating waves, far-field measurements, and computer post-processing.

©2010 Optical Society of America

OCIS codes: (110.3010) Image reconstruction techniques; (160.3918) Metamaterials; (230.1950) Diffraction gratings

Subwavelength focusing of electromagnetic waves is of interest in broad class of applications spanning all parts of electromagnetic spectra. Some applications of subwavelength focusing include nanoimaging, nanolithography, compact photonic elements, and ultra-potent sensors. Metamaterials and plasmonic systems promise to conquer the diffraction limit and offer numerous solutions to the problem of subwavelength imaging [1]. However, while the subwavelength light management in metamaterial systems may be free from diffraction limit, finite-wavelength of light in vacuum provides substantial challenges in experimental studies of nanophotonics. Although near-field measurements [2] provide a way to analyze subwavelength field distributions, these techniques suffer from nontrivial convolution of the field pattern with tip function. Moreover, near-field microscopy is generally not available at IR and THz parts of the spectrum. Here we present a technique that can be used to determine the resolution of subwavelength focusing systems with far-field measurements.

The technique relies on carefully designed grating to convert the information about subwavelength features into the propagating waves, similar to the technique proposed in [3]. However, in contrast to [3], our technique does not rely on resonant enhancement of subwavelength information with plasmonic structures. We illustrate the developed formalism on the example of restoration of subwavelength focal spot of the anisotropy-based planar focusing structure – hypergrating [4], and present generalization for reconstructing any unknown subwavelength images [5].

The fundamental difference between the diffraction-limited and subwavelength images is seen in the wavevector space. The spectrum of the subwavelength focal spot is dominated by high-wavenumber components that exponentially decay away from the focal spot. The grating, that plays the role of image-reconstructing structure, located at the image plane [Fig. 1(a)], converts the evanescent waves into the propagating waves as described [6] by

$$k' = k_0 + mk_\Lambda, \quad (1)$$

where $k_0 = \omega/c = 2\pi/\lambda_0$ is the incident field wavevector, m is the diffraction order, $k_\Lambda = 2\pi/\Lambda$ is the grating wavevector parallel to itself, Λ is the grating period, and k' is the diffracted wavevector. The general design concept that governs the design of the grating is to suppress all but $m = \pm 1$ modes and shift the evanescent signals into the propagating regime. This one-to-one wavevector relation makes imaging retrieval possible.

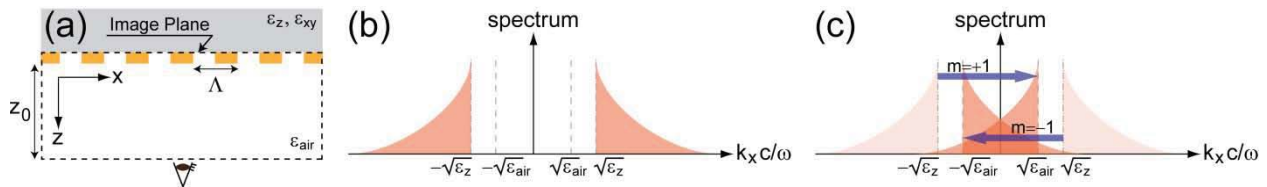


Fig. 1. (a) schematic of the image reconstruction system; the grating is located at the image plane, the measurement is done at the distance z_0 from the grating; (b) spectrum distribution of hypergratings with positive refraction ($\epsilon_{xy} < 0, \epsilon_z > 0$) at the focal point composed of only subwavelength information ($|k_x c / \omega| \geq \sqrt{\epsilon_z}$); (c) the range of high wavevector waves are shifted into the interval of low wavevector waves ($|k_x c / \omega| \leq \sqrt{\epsilon_{air}}$) with $m = \pm 1$ diffraction modes; the length of arrows corresponds to $k_\Lambda c / \omega$;

The spectrum distribution of hypergratings with positive refraction metamaterial ($\epsilon_{xy} < 0, \epsilon_z > 0$) [4,7] is shown in Fig. 1(b). Note that this kind of material only allows the propagation of p-polarized waves. In this work, we let z axis be the propagating direction perpendicular to the alignment of the grating and x and y axes be the

direction parallel to the grating. With this metamaterial, the subwavelength signal occupies only high wavevector information which is immeasurable in far-field vacuum. However, with the assistance of the grating located at the focal plane, we may convert the evanescent waves into the propagating waves which are detectable in vacuum [Fig. 1(c)]. The far-field magnetic field is described as

$$H_y(x, z) = \int_{\sqrt{\epsilon_{air}}\omega/c}^{\sqrt{\epsilon_{air}}\omega/c + k_\Lambda} dk_x a_{-1}(k_x) \exp[i(\alpha_{-1}(k_x)x + k_{z,-1}(k_x)z)] \\ + \int_{-\sqrt{\epsilon_{air}}\omega/c}^{-\sqrt{\epsilon_{air}}\omega/c + k_\Lambda} dk_x a_{+1}(k_x) \exp[i(\alpha_{+1}(k_x)x + k_{z,+1}(k_x)z)] \quad (2)$$

where $\alpha_{\pm 1}(k_x) = k_x \pm k_\Lambda$ and $k_{z,\pm 1}(k_x) = \sqrt{\epsilon_{air}(\omega/c)^2 - \alpha_{\pm 1}^2}$. $a_{\pm 1}(k_x)$ are unknown transmission coefficients of diffracted waves. Note that the range of wavevector integration covers all propagating regimes and some of evanescent regimes. The transmission coefficients are determined from measuring of the field intensity at a distance z_0 from the grating and then fitting it with the intensity function $I(x, z_0) = |H_y(x, z_0)|^2$. There are many numerical techniques, such as curve fitting and interpolation method, which would support this fitting case [8].

When the amplitudes of the transmitted waves are experimentally measured, we Fourier transform Eq. (2) and shift the wavevector back by k_Λ . Subwavelength image information is retrieved by inverse-Fourier transformation. The agreement of our retrieval technique and finite-element method (FEM) simulation [9] is shown in Fig. 2(a).

We confirm the robustness of the approach by reconstructing the image of single slits with width $a = \lambda_0/20$, $\lambda_0/4$, and $\lambda_0/2$ located in an isotropic material. This case is different from the previous one because the spectrum distribution covers not only the evanescent regimes, but also the propagating regimes. Therefore, in order not to mix the propagating and evanescent modes, one may use the rigorously coupled wave analysis (RCWA) technique [10] to design a grating which can suppress $m = 0$ mode and magnify $m = \pm 1$ modes. Following the procedure, Fig. 2(b-d) compares the results from our method and FEM simulations.

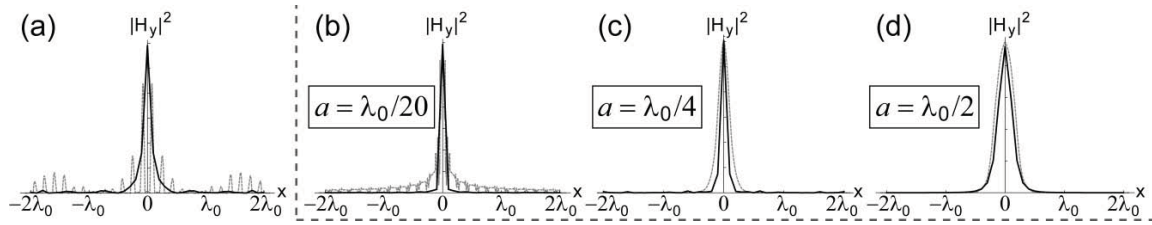


Fig.2. (a) image on the focal plane of the hypergratings; dashed and smooth curves correspond to “numerical experiments” and our retrieval technique, respectively; (b-d) retrieval of single slits with width $a = \lambda_0/20$, $\lambda_0/4$, and $\lambda_0/2$ in the isotropic material, respectively;

To conclude, we proposed an approach to determine the size of the (subwavelength) focal spots with far-field measurements and computer post-processing. The approach, that utilizes a pre-designed diffraction grating located at the focal spot, is easily applicable to majority of subwavelength focusing systems, including metamaterials and plasmonic structures.

This work has been partially supported by ONR (grant #N00014-07-1-0457), NSF (grant #ECCS-0724763), and AFOSR (grant #FA9550-09-1-0029).

References

- [1] J. B. Pendry, Phys. Rev. Lett. **85**, 3966 (2000); Z. Jacob *et al.*, Opt. Exp. **14**, 8247 (2006)
- [2] E. A. Ash and G. Nicholls, Nature **237**, 510 (1972); A. Lewis *et al.*, Ultramicroscopy **13**, 227 (1984)
- [3] S. Durant *et al.*, J. Opt. Soc. Am. B **23**, 2383 (2006); Z. Liu *et al.*, Nano Lett. **7**, 403 (2007); Z. Liu *et al.*, Opt. Exp. **15**, 6947 (2007)
- [4] S. Thongrattanasiri and V. A. Podolskiy, Opt. Lett. **34**, 890 (2009)
- [5] S. Thongrattanasiri *et al.*, in preparation
- [6] M. Born and E. Wolf, *Principles of Optics* (Cambridge U. Press, 1999)
- [7] P. A. Belov, Micro. Opt. Tech. Lett. **37**, 259 (2003); R. Wangberg *et al.*, J. Opt. Soc. Am. B **23**, 498 (2006)
- [8] W. H. Press *et al.*, *Numerical Recipes in Fortran 77* (Cambridge Univ. Press, 1992)
- [9] For details see COMSOL Multiphysics User’s Guide and RF Module User’s Guide; COMSOL AB. (1994-2009); www.comsol.com
- [10] M. G. Moharam and T. K. Gaylord, J. Opt. Soc. Am. **71**, 811 (1981)

Analytical technique for subwavelength far field imaging

Viktor A. Podolskiy^{1,3,*}, Sukosin Thongrattanasiri¹, Nicholas Kuhta¹, Anthony J. Hoffman², Matthew Escarra², Claire F. Gmachl²

¹Department of Physics, Oregon State University, 301 Weniger Hall, Corvallis, OR 97331, USA

²Department of Electrical Engineering, Princeton University, Engineering Quadrangle, Olden Street, Princeton, NJ 08544, USA

³Department of Physics and Applied Physics, University of Massachusetts Lowell, One University Avenue, Lowell, MA 01854, USA

*viktor_podolskiy@uml.edu

Abstract: We develop a computational technique for imaging with subwavelength resolution based on far-field intensity measurements.

High-resolution imaging is of interest for a broad class of applications spanning all parts of the electromagnetic spectrum. Unfortunately, conventional far-field imaging is fundamentally limited by the free-space wavelength. The diffraction limit can be halved with structured illumination microscopy where the spectrum of the incident light is effectively doubled via interference[1]. Alternatively, in the far-field superlens, part of the evanescent radiation emitted by an object is resonantly enhanced via surface plasmon polaritons, and is subsequently converted into propagating waves with a subwavelength diffraction grating[2]. Both techniques rely on multiple measurements and numerical reconstruction algorithms to perform imaging of an unknown object and achieve $\sim \lambda_0/4$ resolution. Here we present an approach capable of *non-resonant* imaging with resolution on the order of $\lambda_0/20$ with far-field measurements[3].

The fundamental difference between the diffraction-limited and subwavelength images is seen in wavevector space. The spectrum of a subwavelength focal spot is dominated by high-wavenumber components that exponentially decay away from the focal spot. The grating, that plays the role of image-reconstructing structure, located at the image plane, and translates the spectrum of the source according to

$$k' = k_0 + mk_\Lambda, \quad (1)$$

where $k_0 \leq \omega/c = 2\pi/\lambda_0$ is the incident field wavevector, m is the diffraction order, $k_\Lambda = 2\pi/\Lambda$ is the grating wavevector, Λ is the grating period, and k' is the diffracted wavevector. Note that diffraction gratings can convert the originally evanescent information into propagating waves which can be measured in the far field. Provided that the far-field measurements of the same object are performed for different values of incident angle (different values of k_0), the contributions of different diffraction orders to the final intensity distribution can be separated from each other, and the original field distribution can be calculated. Typical examples of the restored intensity distribution of subwavelength objects are shown in Fig. 1.

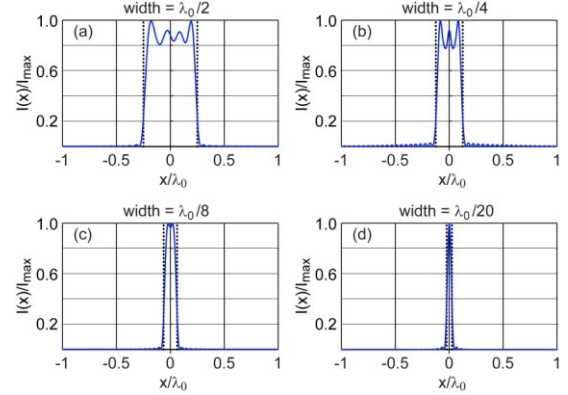


Fig.1. solid lines: images of single-slit sources of different sizes, obtained with the developed technique

This work has been partially supported by ONR (grant #N00014-07-1-0457), NSF (grant #ECCS-0724763), and AFOSR (grant #FA9550-09-1-0029).

References

- [1] E. A. Ash and G. Nicholls, Nature **237**, 510 (1972); A. Lewis *et al.*, Ultramicroscopy **13**, 227 (1984)
- [2] S. Durant *et al.*, J. Opt. Soc. Am. B **23**, 2383 (2006); Z. Liu *et al.*, Nano Lett. **7**, 403 (2007); Z. Liu *et al.*, Opt. Exp. **15**, 6947 (2007)
- [3] S. Thongrattanasiri, N.A. Kuhta, M.D. Escarra, A.J. Hoffman, C.F. Gmachl, and V.A. Podolskiy “Analytical technique for subwavelength far field imaging”, Appl.Phys.Lett. **97**, 101103 (2010)

Analytical technique for subwavelength far field imaging

S. Thongrattanasiri,¹ N. A. Kuhta,¹ M. D. Escarra,² A. J. Hoffman,² C. F. Gmachl,² and V. A. Podolskiy^{3,a)}

¹Department of Physics, Oregon State University, Corvallis, Oregon 97331, USA

²Department of Electrical Engineering, Princeton University, Princeton, New Jersey 08544, USA

³Department of Physics and Applied Physics, University of Massachusetts–Lowell, Lowell, Massachusetts 01854, USA

(Received 1 July 2010; accepted 16 August 2010; published online 7 September 2010)

We develop an analytical technique for retrieving the size and shape of subwavelength objects using far-field measurements. The approach relies on subwavelength diffraction gratings scattering evanescent information into the far field along with a numerical algorithm that is capable of deconvoluting this information based on the far-field intensity measurements. Several examples are presented, demonstrating resolution on the order of $\lambda_0/20$. The developed method can be used at any frequency range, and may become a practical alternative to scanning near-field microscopy.

© 2010 American Institute of Physics. [doi:10.1063/1.3487779]

High-resolution imaging is of interest for the broad class of applications spanning all parts of electromagnetic spectrum. These applications include real-time biomolecule imaging, nanolithography, high capacity optical data storage systems, and compact integrated optical telecom solutions.^{1–5} Electromagnetic metamaterials and plasmonic systems promise to conquer the diffraction limit and offer numerous solutions to the inherent imaging constraints caused by the diffraction limit.^{6–9} However, metamaterials alone may not be perfect solutions to the problem. Indeed, while the light management inside metamaterial systems may be free from diffraction, the finite wavelength of light in vacuum provides substantial challenges in the experimental studies of nanophotonics in free space.

Although near-field scanning optical microscopy^{10,11} provides a way to analyze subwavelength field distributions, this technique suffers from nontrivial convolution of the field pattern with the tip function. It is also implicitly slow and does not support real-time imaging since the evanescent signal is collected on a point-by-point basis. Moreover, near-field microscopy is limited to the optical and gigahertz parts of the spectrum and is not available at mid- and far-IR and terahertz frequencies. Another technique, called structured illumination microscopy (SIM),^{12,13} was shown to improve the resolution of conventional optics by a factor of two by analyzing the light transmitted through a wavelength-scale diffraction grating, under a set of different illumination conditions. More recently, an approach called the far field superlens (FSL) that combines the resonant field enhancement of near-field superlens^{6,14} with the scattering of (subwavelength) surface plasmons into the propagating spectrum has been presented in Refs. 15 and 16. Here we present a technique that combines the benefits of subwavelength resolution of the FSL with the broadband performance of the SIM and can be used to provide real-time imaging of unknown subwavelength objects in the far-field with resolution on the order of $\lambda_0/20$ but is free of SIM and FSL limitations.

We demonstrate the developed formalism by recovering the shape and size of several single and double slit-sources,

and suggest an application of the approach for restoration of the field at the subwavelength focal spot of the anisotropy-based planar focusing structure—hypergrating.⁹ Our analytical results are compared with finite-element-method (FEM) simulations¹⁷ with good agreement.

The fundamental difference between the diffraction-limited and subwavelength images is seen in wavevector space. The spectrum of a subwavelength object is dominated by high-wavenumber components that exponentially decay away from the object. Measurement of these evanescent components is impossible in the far-field regime. However, a subwavelength grating, located at the object plane [Fig. 1(a)], can potentially help the image-reconstructing procedure by converting evanescent waves into propagating waves.¹⁸ The wavevector of the scattered wave q_m would be related to the wavevector k_x of the incident wave by

$$q_m = (k_x - k_{x0}) + mk_\Lambda, \quad (1)$$

where k_{x0} is the parallel-to-grating component of the wavevector of the incident field, m is the integer diffraction order, Λ is a (subwavelength) period of the grating, and $k_\Lambda = 2\pi/\Lambda$ [see Fig. 1]. In a sense, the subwavelength grating shifts portions of the evanescent spectra into the propagating regime [Fig. 1(b)], where the originally evanescent components could be detected with far-field measurements. This procedure, however, leads to overlapping of the original evanescent signals with originally propagating waves; so that extra measurements are required to deconvolute the different

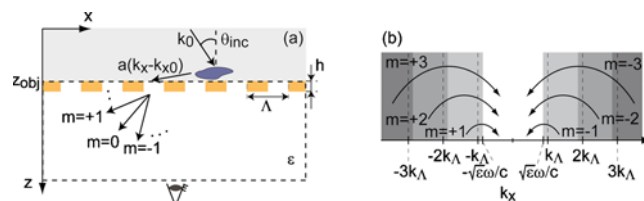


FIG. 1. (Color online) (a) Schematic of the imaging configuration; an object is placed close to the subwavelength plasmonic grating with period Λ (at $z \approx z_{\text{obj}}$) and is irradiated by a plane wave with incident angle θ_{inc} ; the far-field intensity is measured inside the material with permittivity ϵ . (b) Transfer of evanescent information into propagating regime by the m th diffraction order of the grating; normal incidence is assumed.

^{a)}Author to whom correspondence should be addressed. Electronic mail: viktor_podolskiy@uml.edu.

parts of the spectra from the far-field measurements. Both SIM and FSL rely on the rotation of polarization of incident light to attain additional measurements to perform the above deconvolution. This procedure, however, is not desirable for systems where the properties of the sample strongly depend on polarization. Here we propose to *fix the polarization* of incident light, and instead *rotate its direction* (given by the angle of incidence θ_{inc}) as shown in Fig. 1(a). The set of measurements corresponding to different values of θ_{inc} is then postprocessed with a numerical algorithm to restore the unknown object.

Computationally, the problem of imaging can be reduced to the problem of finding the unknown (complex) amplitudes $a(k_x)$ of the Fourier decomposition of the light scattered by the object at the $z=z_{\text{obj}}$ plane as follows:

$$H_y^{\text{obj}}(x, z_{\text{obj}}) = \int_{-\infty}^{\infty} dk_x a(k_x) \exp(ik_x x) \exp[ik_z(k_x) z_{\text{obj}}], \quad (2)$$

where the z -component of the wavevector k_z is related to k_x through the dispersion relation.¹⁸ It is straightforward to show that light propagating behind the grating is described by

$$H_y(x, z, \theta_{\text{inc}}) = \sum_m \sum_n w_n a(k_{x,n} - k_{x0}) t_m(k_{x,n} - k_{x0}) \exp(iq_{mn}x) \exp[ik_z(q_{mn})z], \quad (3)$$

where $q_{mn} = (k_{x,n} - k_{x0}) + mk_{\Lambda}$, $k_z(q_{mn}) = \sqrt{\epsilon \omega^2/c^2 - q_{mn}^2}$, and ϵ is the permittivity of the (isotropic) medium where the field is measured. The index m corresponds to the summation over different diffraction orders while the index n represents the numerical integration over k_x with weighting factors w_n [Fig. 1(b)].¹⁹ The efficiency of evanescent-to-propagating light conversion by a diffraction grating is given by the optical transfer function t_m defined as

$$t_m(k_{x,n} - k_{x0}) = \frac{a(q_{mn})}{a(k_{x,n} - k_{x0})}, \quad (4)$$

where $a(k_{x,n} - k_{x0})$ and $a(q_{mn})$ are amplitudes in front of ($z < z_{\text{obj}}$) and behind ($z > z_{\text{obj}}$) the grating, respectively. The transfer function is assumed to be a known quantity; in our work, t_m is computed by the rigorously coupled wave analysis technique.²⁰ Our calculations show that the grating with $\Lambda = 2\lambda_0/3$ provides substantial coupling between propagating modes and evanescent spectrum covered by the first seven diffraction orders which potentially yields a resolution of $\lambda_0/20$; better resolution may be achievable with further optimization of the grating parameters.

To determine the unknown transmission coefficients $a(k_{x,n} - k_{x0})$ we fit the experimentally measured intensity distribution in the far field, $I_p = |h_p|^2$, for a set of values of θ_{inc} to Eq. (3) using the nonlinear least-squares fitting technique based on the Gauss–Newton algorithm²¹ by minimizing the difference

$$F = \sum_{p=1}^P [I_p - |H_y(x_p, z_p, \theta_{\text{inc},p})|^2]^2, \quad (5)$$

where the summation is extended over P data points $\{\theta_{\text{inc},p}, x_p, z_p, h_p\}$. Assuming that $k_{x,n}$ is smaller than a cutoff wave vector $k_{x,\text{max}}$, the unknown transmission coefficients can be represented by following Taylor series:

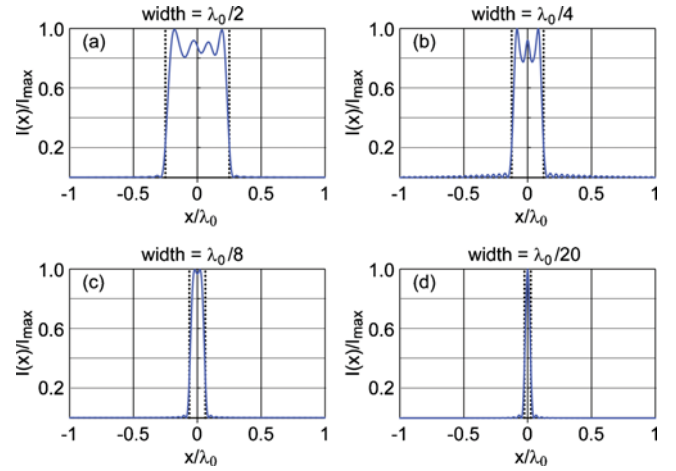


FIG. 2. (Color online) Reconstruction (solid curves) of single slits with width (a) $\lambda_0/2$, (b) $\lambda_0/4$, (c) $\lambda_0/8$, and (d) $\lambda_0/20$; dotted lines represent the object size; vacuum-to-vacuum measurement is assumed.

$$a(k) = a_0 + a_1 k^1 + \dots + a_j k^j + \dots \quad (6)$$

Finally, once the spectrum of the source is determined, the object is recovered using Eq. (2).

We now illustrate the developed formalism by considering the imaging of several single-slit sources with widths $a = \lambda_0/2, \lambda_0/4, \lambda_0/8$, and $\lambda_0/20$ and double slit-slit sources with two $\lambda_0/4$ slits separated by $\lambda_0/5$. We assume that all linear dimensions are normalized to the free-space wavelength λ_0 , and use the following parameters for the plasmonic grating: permittivity $\epsilon_g = -100$, thickness $h = \lambda_0/10$, metallic filling factor $f = 0.5$, and grating period $\Lambda = 2\lambda_0/3$. To simulate experimental conditions, we calculate the intensity behind the grating using a commercial software that implements FEM solutions of Maxwell's equations,¹⁷ and use the calculated intensity as “experimental” input field I_p . The good agreement of our retrieval technique for single and double slits and their original configurations is shown in Figs. 2, 3, and 4(a).

We further apply the developed formalism to recover the field distribution in the focal plane of the planar subwavelength focusing device based on strongly anisotropic (hyperbolic) metamaterials, known as the hypergrating.⁹ A good agreement between the original and recovered fields is found

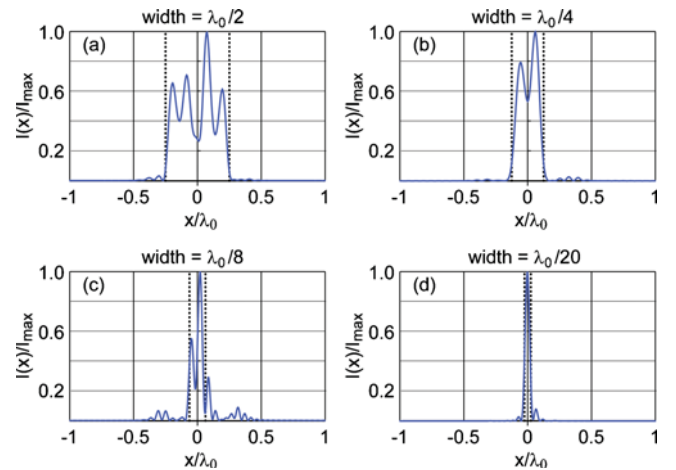


FIG. 3. (Color online) Reconstruction (solid curves) of single slits [as in Fig. 2] with a random 2% noise included.

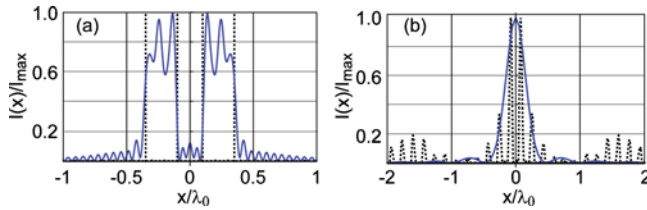


FIG. 4. (Color online) (a) Reconstruction of two $\lambda_0/4$ slits separated by $\lambda_0/5$ (vacuum-to-vacuum measurement). (b) Reconstruction of the subwavelength focal spot of the hypergrating based on measurement in vacuum; solid and dotted curves correspond to retrieved and original images, respectively.

when using a grating with parameters $\varepsilon_g = -12\,962.6 + i3726.0$,²² $h = \lambda_0/80$, $f = 0.5$, and $\Lambda = \lambda_0/(\sqrt{\varepsilon_z} + \sqrt{\varepsilon_0})$, corresponding to Cu at $\lambda_0 = 20\,\mu\text{m}$. Note that the particular hypergrating system, having $\varepsilon_{xy} = -23.25 + i3.65$ and $\varepsilon_z = 24.84 + i0.69$, used in our simulations suppresses small k_x components of the field (see Ref. 9 for more details), so that the image recovery can be achieved with a single θ_{inc} measurement.

Finally, we analyze the tolerance of the developed formalism to imperfections, present in any experiment, by adding a random 2% noise to “experimental” field distributions from single slits, and averaging the field recovered upon several noise realizations. Our simulations demonstrate that the recovered procedure is relatively stable under small perturbations (Fig. 3). Noise tolerance will be the main limiting factor of the proposed technique; it is natural to anticipate that the signals corresponding to higher values of parameter m in Eq. (4) would be more sensitive to imperfections in measurements, as well as to imperfections in fabrication of diffraction gratings.

In conclusion, we have proposed a technique capable of retrieving unknown subwavelength images with far-field measurements by using a diffraction grating with subwavelength period and computer postprocessing. As compared with previously introduced techniques, the proposed approach is implicitly nonresonant, and thus provides a rela-

tively large operating bandwidth. It also enables subwavelength resolution ($\leq \lambda_0/20$), and opens the door for real-time imaging.

This work has been partially supported by ONR (Grant No. N00014-07-1-0457), NSF (Grant No. ECCS-0724763), and AFOSR (Grant No. FA9550-09-1-0029).

¹R. Weissleder and U. Mahmood, *Radiology* **219**, 316 (2001).

²Z. W. Liu, Q. H. Wei, and X. Zhang, *Nano Lett.* **5**, 957 (2005).

³W. Sritravanich, N. Fang, C. Sun, Q. Luo, and X. Zhang, *Nano Lett.* **4**, 1085 (2004).

⁴B. D. Terris, H. J. Mamin, and D. Rugar, *Appl. Phys. Lett.* **68**, 141 (1996).

⁵B. H. Cumpston, S. P. Ananthavel, S. Barlow, D. L. Dyer, J. E. Ehrlich, L. L. Erskine, A. A. Heikal, S. M. Kuebler, I. Y. S. Lee, D. McCord-Maughon, J. Q. Qin, H. Rockel, M. Rumi, X. L. Wu, S. R. Marder, and J. W. Perry, *Nature (London)* **398**, 51 (1999).

⁶J. B. Pendry, *Phys. Rev. Lett.* **85**, 3966 (2000).

⁷M. I. Stockman, *Phys. Rev. Lett.* **93**, 137404 (2004).

⁸Z. Jacob, L. V. Alekseyev, and E. E. Narimanov, *Opt. Express* **14**, 8247 (2006).

⁹S. Thongrattanasiri and V. A. Podolskiy, *Opt. Lett.* **34**, 890 (2009).

¹⁰E. A. Ash and G. Nicholls, *Nature (London)* **237**, 510 (1972).

¹¹A. Lewis, M. Isaacson, A. Harootunian, and A. Muray, *Ultramicroscopy* **13**, 227 (1984).

¹²R. Heintzmann and C. Cremer, *Proc. SPIE* **3568**, 185 (1998).

¹³M. G. L. Gustafsson, *J. Micro. Oxford* **198**, 82 (2000).

¹⁴R. A. Shelby, D. R. Smith, and S. Schultz, *Science* **292**, 77 (2001).

¹⁵S. Durant, Z. W. Liu, J. A. Steele, and X. Zhang, *J. Opt. Soc. Am. B* **23**, 2383 (2006).

¹⁶Z. W. Liu, S. Durant, H. Lee, Y. Pikus, Y. Xiong, C. Sun, and X. Zhang, *Opt. Express* **15**, 6947 (2007).

¹⁷For details see COMSOL Multiphysics 3.4 User's Guide and RF Module User's Guide, www.comsol.com.

¹⁸M. Born and E. Wolf, *Principles of Optics* (Cambridge University Press, Cambridge, 1999).

¹⁹W. H. Press, B. P. Flannery, S. A. Teukolsky, and W. T. Vetterling, *Numerical Recipes in FORTRAN77* (Cambridge University Press, Cambridge, 1992).

²⁰M. G. Moharam, E. B. Grann, D. A. Pommet, and T. K. Gaylord, *J. Opt. Soc. Am. A* **12**, 1068 (1995).

²¹C. T. Kelley, *Iterative Methods for Optimization* (SIAM, Philadelphia, 1999).

²²*The Handbook of Optical Constants of Solids*, edited by E. D. Palik (Academic, New York, 1997).